Thermally-Actuated Piezoresistively-Sensed Mechanical Silicon Oscillator

by

Subramanian Sundaram

Submitted to the Department of Electrical Engineering and Computer
Science
in partial fulfillment of the requirements for the degree of

Master of Science in Electrical Engineering and Computer Science

at the

MASSACHUSETTS INSTITUTE OF TECHNOLOGY

February 2014

© Massachusetts Institute of Technology 2014. All rights reserved.

Author . . . .
Department of Electrical Engineering and Computer Science
January 9, 2014

Certified by . . . .
Dana Weinstein
Associate Professor of Electrical Engineering and Computer Science
Thesis Supervisor

Accepted by . . . .
Leslie Kolodziejski
Professor of Electrical Engineering
Chairman, Department Committee on Graduate Theses

Thermally-Actuated Piezoresistively-Sensed Mechanical Silicon Oscillator

by

Subramanian Sundaram

Abstract

In the past two decades, Microelectromechanical (MEMS) resonators have emerged as front runners for RF front-ends, high frequency filters, and frequency sources in various applications. The prospect of seamless integration with CMOS has provided a significant boost to displace Quartz, which for long has been the go-to option for timing sources. To construct an oscillator, a MEMS resonator is operated with an active feedback amplifier, the design of which can be a major challenge at high frequencies. In this work we implement a self sustaining mechanical Si oscillator that has an internal feedback mechanism. The oscillator is based on a thermal actuation mechanism due to the Joule heating effect caused by running currents through narrow channels. These narrow channels when oriented along the <100>direction in an n-doped Si wafer, show large negative piezoresistance coefficients. Beyond significant threshold DC current densities (GA/m^2), the thermal-actuation and piezoresitive-feedback loop excite the mechanical structure, causing spontaneous oscillations. We begin with the investigation of scaling trends based on an equivalent circuit model of the device. Targeting high frequency oscillators, we design suitable geometries and discuss the microfabrication processes used to fabricate these devices. Finally, we report the experimental results of the fabricated devices.

Thesis Supervisor: Dana Weinstein
Title: Associate Professor of Electrical Engineering and Computer Science

Acknowledgments

I am very thankful to my advisor Prof. Dana Weinstein for her guidance, and being an amazing role model. Her vast knowledge of MEMS, and her ability to ask the most relevant questions will continue to inspire me. My initial conversations with her provided me the reasons to come to MIT and I am thankful for that. I have also benefitted greatly from the remarkable teachers at MIT who have made graduate courses very enjoyable and insightful.

Much of my work at MIT revolved around the MTL cleanroom and I am thankful to all the MTL staff for helping me with my process and traning me on the available tools. I am thankful to Nikon for making the Stepper which continues to be a dragon that hasn't been tamed. I am grateful to my friends at the cleanroom for being helpful and sharing their own cleanroom tricks. I'm also thankful to my helpful labmates for providing various initial simulation files and help, and some great company.

Prof. Herbert Shea, my undergraduate thesis advisor, at the Ecole Polytechnique Fédérale de Lausanne has been a great friend and mentor. I have learnt many life lessons from him. His cheerful promptness and ability to think objectively in a selfless manner stuns me, as I continue to seek his help when I face difficult choices. Dr. Kannan Balasubramanian at the Max Planck Institute of Solid State Research, my other undergraduate thesis mentor, introduced me to inspiring fundamental science research, and together with other friends, he demonstrated how to have fun doing it. Thanks very much Herb and Kannan for showing me that it is fun doing research. My interests in MEMS and fabrication were sparked by my professors Prof. N. N. Sharma and Prof. R. Mehrotra during my undergraduate days. I am indebted to Prof. Sharma for having faith in me, for teaching me MEMS and the initial skills I needed for research, and going out of his way to clear administrative roadblocks for me.

I am deeply thankful to my mother and grandmother for having immense clairvoyance, teaching me how to face challenges and adversity, and for always supporting me even when it meant making a lot of sacrifices on their part.

என்னை உருவாக்கிய என் அம்மா மற்றும் பாட்டிக்கு

Contents

List of Figures

9

11

List of Tables

Chapter 1

Introduction

Frequency sources, clocks for logic circuits and synchronizing sources for data transmission are ubiquitous in various communication and consumer applications, and in modern day electronics in general. The design of the specific resonators and oscillators suited for these tasks is based on specific requirements of these applications. Most common oscillators today use a mechanical Quartz resonator as the frequency selective element. Recently, radio-frequency (RF) microelectromechanical systems (MEMS) based resonators are acquiring a larger market share due to various advantages, but most importantly due to the possibility of integration with electronic circuitry in the same package[4].

1.1   MEMS timing sources

To create a MEMS clock, the general approach has been to use a micromachined mechanical resonator [5, 6] that is set into sustained oscillations with the aid of an oscillator circuit, which is the feedback loop. On-chip RF MEMS resonators have now reached significant levels of maturity after several iterations by research groups in academia and commercial companies. MEMS oscillators have very effectively bridged the gap between high performance Quartz based references and low performance on-chip electrical oscillators, and over the past decade, have rivalled Quartz based timings sources in all metrics such as power dissipation, frequency stability and frequency

accuracy [7]. At the heart of every MEMS oscillator is a high performance MEMS resonator which also offers an improved possibility of integration and miniaturization. Best reported Frequency-Quality factor products ($f.Q$, which is the common figure of merit for resonators) have consistently reached 10^{13}-10^{14}.

1.2   RF MEMS

Different components such as RF switches, varactors, tunable inductors and resonators make up the entire toolkit of RF MEMS. Resonators play an important role as they can be used to make various filters, frequency selective elements for clocks, and high-power front ends.

1.2.1   Resonator Specifications

In most cases for timing and clocking applications, resonators work in unison with an oscillator circuit, and it is necessary to look at them simultaneously while defining the target specifications. Overall, there has been a targeted effort to reduce the total power consumption, decrease phase noise, improve long term frequency stability while exploring various transduction mechanisms and device geometries that lead to a minimal motional impedance and low input impedance . Resonators with low motional impedances and large quality factors simplify the task of building oscillator circuits operating with closed loop unity gain feedback at the required frequency and phase shift. The following are some important parameters and properties:

- Quality factor, Q: the quality factor denotes the sharpness of the frequency response of a resonator, and the extent of under-damping in a system. It can also be described as the ability to retain energy with less dissipation. The requirements for Q depend on the application, for example, resonators used in clocks require high Qs.

- Motional impedance, R_X [Ω]: the motional impedance of a resonator is the ratio of the input voltage to the output current, and represents the efficiency

of transduction from input to output. Low values of R_X, indicating better transduction efficiencies, simplify the requirements from the electronic amplifier required for an oscillator [8].

- Temperature coefficient of frequency (TCF): TCF denotes the sensitivity of the resonant frequency to changes in temperature. Smaller values leads to an improved frequency stability in the presence of thermal fluctuations [9].

- Frequency accuracy: High frequency accuracy indicates the ability to reach a set frequency, and this quality become important in applications that require synchronization.

Other factors like the power handling capacity (ability of withstand large input power and deformations while behaving linearly), easy tuning of the frequency, and scalability are also important properties [10].

1.3   Piezoresistive-Thermal Oscillators

Recently, a new kind of MEMS oscillator that has an internal feedback mechanism that obviates the need to build feedback circuits has been demonstrated [7, 1, 11]. The device can be described as a thermally-actuated piezoresistively-sensed oscillator with an inherent closed loop feedback path.

The oscillator is defined using a single mask fabrication procedure on the device layer of an SOI wafer, and is released by removing the underlying buried oxide. The device essentially consists of a narrow beam also called the actuator, and other structures that make up the resonator. Figure 1-1 shows a schematic of the narrow actuating beam, the proof mass and the wide beam that acts at the mechanical spring. The large currents (and current densities) flowing through the actuator causes it to expand as a result of Joule heating. The elongation of the beam, oriented along the [100] direction, causes the resistance to drop due to the large negative longitudinal piezoresistive coefficient. This drop in the resistance, leads to a reduction in the heat generated at the beam. The reduction in heat input causes a correction in the
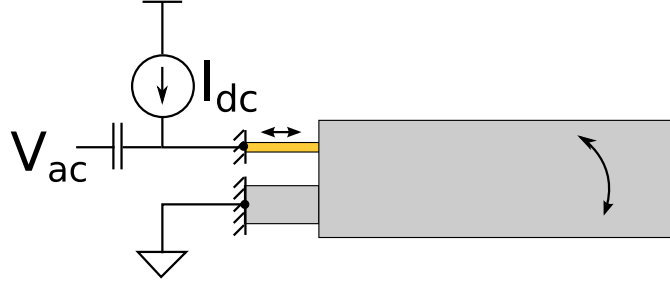
Figure 1-1: Schematic of the flexural mode oscillator (based on [1]). The narrow beam actuator (in orange) is oriented along [100], and actuated thermally by the current flowing through it. This causes flexural mode oscillations of the proof mass about the wide beam which acts as the spring. The output voltage is read at the input terminal through a capacitor to block the DC voltage.

length of actuator. This entire process occurs repeatedly and constitutes the feedback mechanism. It can now be seen as an actuator that expands and contracts periodically, and when this matches the resonant frequency of the resonator, it is driven into sustained oscillations with large amplitudes. The product of the DC bias current, I_{dc} and the modulation in the resistance r_{ac} appears as the output voltage V_{ac}. When the threshold current density $J_{th} = 2.83 \ GA/m^2$ is reached, the feedback mechanism compensates the energy lost per cycle, and the device spontaneously oscillates at 1.26 MHz. This device is generally limited to low frequencies due to the nature of the mode.

Subsequently, a 6.6 MHz extensional dual plate mode based oscillator was demonstrated using the same fundamental principle [12]. Improving on the design, oscillators with frequencies up to 161 MHz have been fabricated [2]. Figure 1-2 shows the extensional dual plate mode oscillator (I-bar oscillator), where the four actuators act as both the actuation elements, and set the stiffness of the resonator. The two proof masses and the four actuators are freely suspended. The current splits equally among the two branches and flows through the two masses. This causes the four actuators to expand and contract, using the same feedback mechanism described earlier, leading to sustained oscillations. Further, using a similar geometry, two modes have been excited simultaneously, using the bias current to control the nonlinearity in the device [13]. The geometry of these devices allows them to be used in sensing
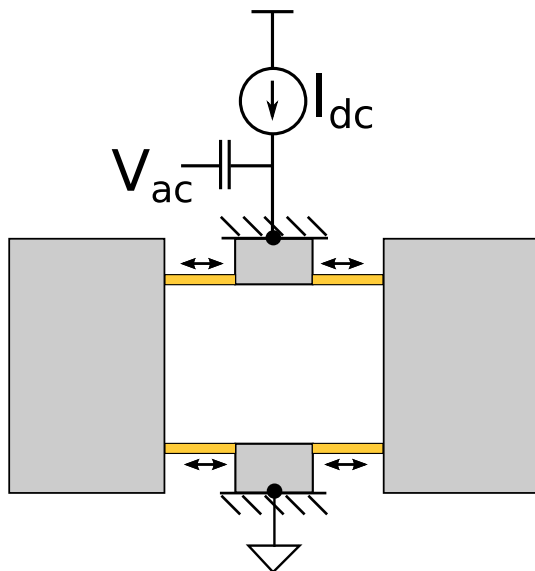
Figure 1-2: Schematic of the extensional dual plate oscillator (based on [2]). The four actuators (in orange) cause the two proof masses to vibrate horizontally.

applications [14].

There are several factors that make this oscillator promising. The footprint is effectively the same as that of the resonator, with the supports used to suspend the mechanical resonator acting as actuators. Importantly, no additional feedback circuitry is required. The inherent feedback mechanism automatically tracks any changes in the resonance frequency and adjusts the phase, provided the oscillation threshold is attained. All of this comes at a cost of very high current densities, leading to high power consumption.

The upper limits of frequencies attainable is still not clear, and there is little understanding on how to push these limits. The devices demonstrated so far are quite similar in nature: the relevant mechanical stiffness and the mass have been isolated, and pure bulk mode oscillators have not been realized. One of the major goals of this thesis is to explore different bulk mode geometries in an attempt to reach higher frequencies. An analytical model is built to understand the effects of varying the thermal and mechanical time constants. These results are used to create device designs with smaller threshold current densities and lower power requirements. The model is extended to investigate the general efficiency of these oscillators as device dimensions

are scaled. The working principle of these oscillators, the equivalent circuit model, and the overall analytical framework are discussed in chapter 2. The fabrication techniques used to create these devices, with details of independent steps is described in chapter3. Results from analytical calculations, and experimental measurements are detailed in chapter 4. Finally, chapter 5 summarizes the results obtained and presents a set of possible directions for future work.

Chapter 2

Silicon Piezoresistive-Thermal Oscillator: Device Design and Equivalent Circuit Model

The mechanical oscillator described here requires the thermal, piezoresistive and mechanical loops to work in unison, and satisfy the Barkhausen criteria [1, 11]. Each of these can be carefully engineered to improve the performance of the oscillator. The final oscillator's quality is a function of the design and the fabrication process.

This chapter starts by discussing the general working principle and the factors affecting the various sub-blocks. The equivalent circuit model is developed to analyze the performance of the oscillator. The model is used to understand the effects of varying different parameters, the interplay between the thermal and mechanical loops, and develop scaling trends.

2.1   Working Mechanism

Normally, the functional parts of the oscillator are described in a single mask, which is used to pattern the device layer of an SOI wafer. The underlying buried oxide (BOX) is removed to suspend the actuators and the proof mass. These released parts are free to vibrate, and make up both the frequency selective element and the amplifier of the
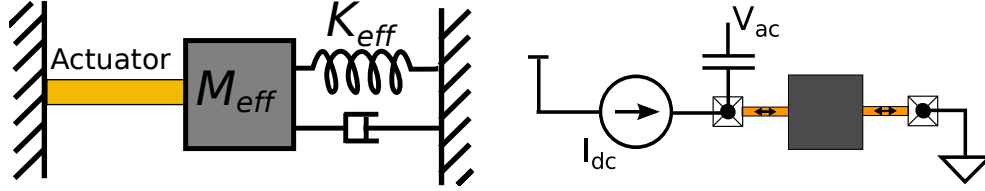
Figure 2-1: (left)Lumped 1D model of the piezoresistive-thermal oscillator showing the thermal actuator, the lumped mass, stiffness and the damping components. (right) Schematic of a Lamé oscillator with 2 actuators. The square mass contributes both M_{eff} and K_{eff} in this case. The DC bias current flows through the actuators and the resonator.

oscillator. The oscillator can thus be modeled as a proof mass attached to a spring (and elements with damping) and an actuator; a simplified schematic of this is shown in figure 2-1. A corresponding schematic of a Lamé mode device with 2 actuators is shown on the right. In this case, the bias current runs through the actuators, and the resonator. The narrow actuator beam can be assumed to contribute negligibly to the overall stiffness of the structure. The frequency of oscillations is entirely set by the value of M_{eff}, K_{eff} and the damping conditions. Once the self-limited amplitude of oscillations in reached, the actuator pumps the same amount of energy that is lost via damping mechanisms, back into the system every cycle.

2.1.1 Piezoresistance in Silicon

Piezoresistance is a phenomenon, seen in some crystalline or non-amorphous materials, which accounts for a change in the resistivity in response to a stress in the lattice. The paper by C. S. Smith was one of the earliest reports highlighting the piezoresistance effect in silicon [15]. In piezoresistive materials the change in resistance from the changes in the geometry are much smaller than the change due to the applied mechanical stress.The effect is prominent in carbon nanotubes [16], semiconductor nanowires [17] and crystalline silicon, where the piezoresistive contribution to resistance change is several orders more than that from geometry changes. The fractional change in resistivity depends linearly on the stress components σ_β, and is expressed

as

$$\frac{\Delta\rho_{e\alpha}}{\rho_e} = \sum_{\beta=1}^{6} \pi_{\alpha\beta}\sigma_\beta \tag{2.1}$$

where σ_β is the component of the stress tensor in six-component vector notation and $\pi_{\alpha\beta}$ is the component of the piezoresistive coefficient tensor [18, 3]. In crystals with cubic symmetry, $\pi_{\alpha\beta}$ is given by

$$[\pi_{\alpha\beta}] = \begin{pmatrix} \pi_{11} & \pi_{12} & \pi_{12} & 0 & 0 & 0 \\ \pi_{12} & \pi_{11} & \pi_{12} & 0 & 0 & 0 \\ \pi_{12} & \pi_{12} & \pi_{11} & 0 & 0 & 0 \\ 0 & 0 & 0 & \pi_{44} & 0 & 0 \\ 0 & 0 & 0 & 0 & \pi_{44} & 0 \\ 0 & 0 & 0 & 0 & 0 & \pi_{44} \end{pmatrix} \tag{2.2}$$

The actual mechanisms involved in the piezoresistance effect and their contributions depend on the material and the nature of the impurity. For e.g., N-type silicon has three pairs of conducting valleys, and a stress in the lattice causes the causes a change in the effective mass. When the material is subjected to an external force, the band edges for a few valleys go up while the others go down. This leads to a rearrangement of electrons between different valleys [19]. There are primarily two kinds of piezoresistive coefficients that need to be considered. The first of them is the longitudinal piezoresistive coefficient when the current flow is in the same direction as that of the applied mechanical stress. In the other case where the effect of change in the resistance is observed along a direction perpendicular to the applied stress, it is accounted for by the transverse piezoresistive coefficient. With the coordinate system aligned with the <100> direction, the piezoresistive coefficients for silicon are listed in table 2.1.

In n-type single crystal silicon (SCS) the longitudinal piezoresistive coefficient is largest (most negative) along the [100] direction [18] and is numerically equal to $-102.2 \times 10^{-11}/Pa$. The negative sign here decides the nature of the feedback. Piezoresistivity becomes less effective and starts to drop at donor concentrations over

| Si material | ρ | π_{11} | π_{12} | π_{44} |
	$(\Omega\ cm)$	$(10^{-11}\ Pa^{-1})$	$(10^{-11}\ Pa^{-1})$	$(10^{-11}\ Pa^{-1})$
Crystalline N-type	11.7	-102.2	53.4	-13.6
Crystalline P-type	7.8	6.6	-1.1	138.1

Table 2.1: Piezoresistive coefficients in silicon (from [3])
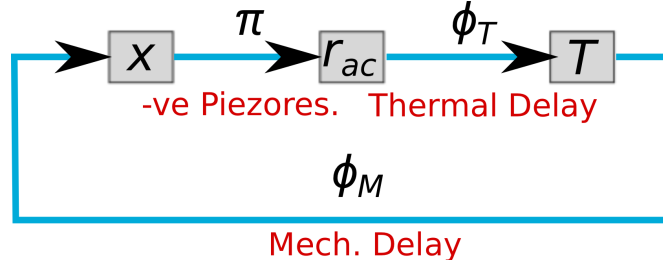
Figure 2-2: Feedback loop showing the displacement x, resistance r_{ac}, and temperature T. π accounts for the sign inversion for the transformation between x and r_{ac}. ϕ_T and ϕ_M are the thermal and mechanical phase shifts.

$10^{19}/cm^3$. The effect also becomes much stronger at lower temperatures: there is a 50% boost as the temperature is lowered from room temperature to 200K [18]. In general the piezoresistance effect observed in silicon is nonlinear [20], but under conditions of small applied stresses, it can be modeled linearly using the piezoresistive coefficient described earlier.

The value and the sign of the piezoresistive coefficient, play a crucial role in the working of the piezoresistive-thermal oscillator. Figure 2-2 shows the feedback loop and the various transformations involved: displacement to change in resistance via the piezoresistance coefficient, change in resistance to change in heat generated via Joule heating, and the change in temperatures leading to displacement via thermal expansion. π denotes the 180° phase shift from displacement to change in the resistance. This stems from the fact that the longitudinal piezoresistive coefficient is negative in n-type silicon along [100]. ϕ_T and ϕ_M denote the phase shift from the thermal and mechanical components.

2.1.2 Joule Heating

Thermal actuation in the device is achieved by the Joule heating effect where a material expands as a result of a rise in temperature, caused by the flow of large currents through it. The thermal power, P_{th}, generated by the flow of current I through a resistive path R_e is given as

$$P_{th} = I^2 R_e \qquad (2.3)$$

The generation of thermal power leads to a change in the temperature (ΔT)

$$\Delta T = P_{th} R_t \qquad (2.4)$$

where R_t is the thermal resistance to a heat sink. Silicon expands isotropically in response to an elevation in temperature. The increase in length (ΔL) is considered to be linear with change in temperature for small deltas, and is written as $\alpha \Delta T L$, where L is the original length, and α is the thermal expansion coefficient. α is temperature dependent and the numerical value increases from $2.6 \times 10^{-6} K^{-1}$ and $4.3 \times 10^{-6} K^{-1}$ between 293K and 1000K [21].

The actuator in any thermally actuated device is generally a narrow and long element that dominates the overall resistance in the current flow path. Thus the heat input is focussed on this region instead of heating all parts of a device uniformly. Typically, micro-thermal actuators generate a large force and displacement, and operate at lower voltages compared to their electrostatic counterparts. Since such actuators merely require a channel for current flow, fabricating these structures is generally straightforward. The time required for actuation is of the order of the thermal time constant of the structure. This has been the limiting factor for high frequency thermal actuation, and places strict constraints on the dimensions of actuators. These factors will be highlighted in the equivalent circuit parameters.

2.2 Resonator Structure

The lumped model in Fig. 2-1 highlights the components required to build an oscillator. The actuator is simply a current carrying narrow beam of silicon. As will be shown later, there are various factors to be considered while designing the actuator. However, the overall device and it's behavior can be greatly improved by carefully engineering the resonator which contributes M_{eff}, K_{eff} and the damping terms. This part of the thesis talks in detail about the different resonator designs used here.

Bulk Acoustic Wave (BAW) resonators and Film Bulk Acoustic Resonators (FBARs) have been popular as frequency sources and are utilized in quartz crystal oscillators, and as filters. Bulk mode devices have been able to reach $f.Q \to 10^{14}$ in single crystal silicon resonators [22]. In general bulk mode devices have larger $f.Q$ products compared to flexural mode resonators, where damping mechanisms such as Thermoelastic Damping (TED) can be dominant [23]. Anchor losses can also be minimized in bulk acoustic resonators by carefully designing the supports at suitable points, and of certain lengths [24]. New techniques to minimize the radiation of acoustic energy through the supports by the utilization of slotted reflectors have also emerged [25]. In the devices we consider here, the supports also perform the role of actuator beams, and the position and length cannot be decided with the sole intention of optimizing the Q. The length of the actuators here decide the thermal time constant, and position of the actuator with respect to the modeshape decides the efficiency of actuation. These two factors will be discussed in greater detail here and in Sec. 2.3.

Over the years, several kinds of bulk mode resonators have been fabricated in silicon. Some of the resonator designs that are considered here in greater detail are the square extensional mode [26], Lamé mode [27], radial and wineglass disk modes [28, 29] and extensional-wineglass ring mode [30, 31]. Figure 2-3 shows the top view of some of the resonator designs that have been fabricated here. In all these devices the effective mass and the stiffness come from the same physical element, called the resonator (in gray). In all these cases, the supports act as the actuation element too, and have to be oriented along any of the equivalent <100> directions to benefit

(a) Lamé mode   (b) Square extensional mode   (c) Radial disk mode

(d) Wineglass disk mode   (e) Extensional wineglass mode
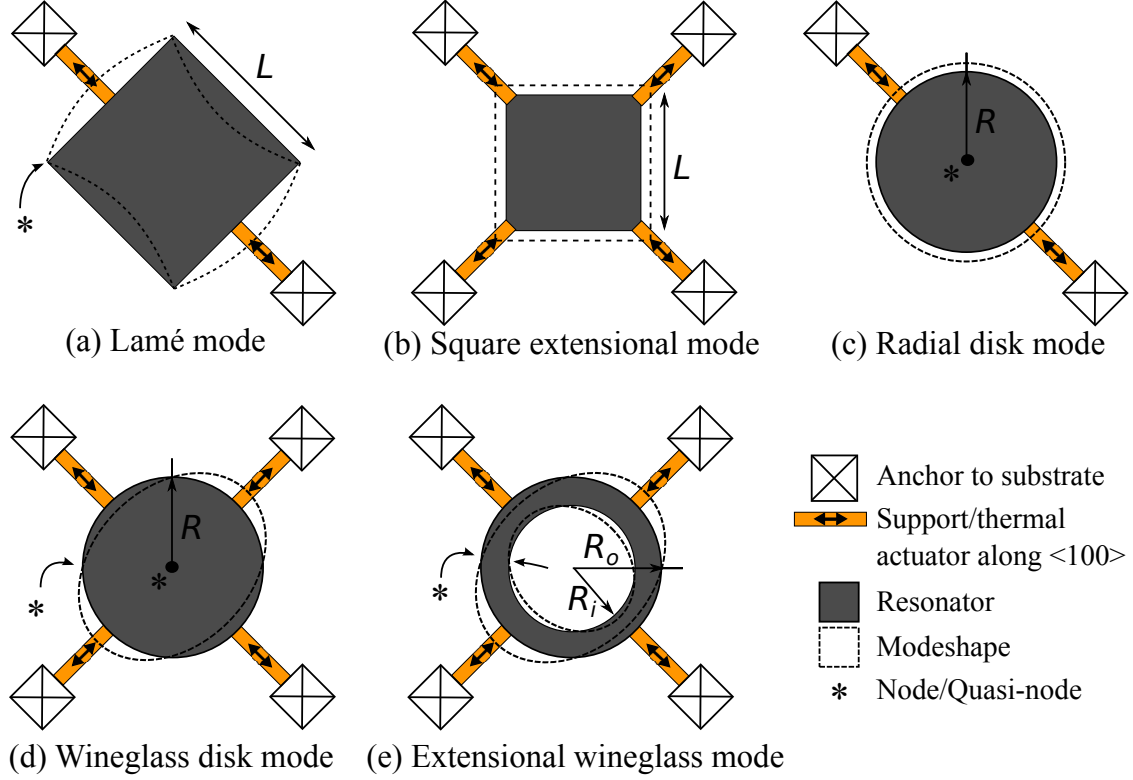
Figure 2-3: Resonator design schematics for the (a) Lamé mode (b) square extensional mode (c) radial disk mode (d) disk wineglass mode and (e) ring extensional wineglass mode. Dashed lines show the mode-shape. The nodes and quasi-nodes are indicated by '*'. The supports and the proof mass are released, and anchored to the substrate at the anchors.

from the large piezoresistive coefficient. In our designs we created structures with 2 and 4 support as shown in the figure. It is to be noted that the actuator and the proof mass (or the resonator) are both etched into the same device layer. Different colors have been used for clarity, but they are of the same thickness, and are made of the same material. Anchors are connected to the BOX, and the handle wafer, rigidly holding the ends of the freely suspended parts. We will now proceed further by looking at these modes in detail, and look at the expressions for the effective mass and the effective stiffness. The variables used in this section, and their definitions are listed in table A.1.

Lamé mode: The Lamé mode is an isochoric mode (i.e. it is volume conserving) that can be excited in rectangularly shaped resonators. The Lamé mode has 4 quasi-nodal points where there is *zero* displacement, and there is maximum displacement at

the centre of the sides for the first order mode as shown in Fig. 2-3. The out-of-phase motion of the adjacent sides has been used to facilitate differential measurements. Sunil et al. report on utilizing an array of coupled Lamé mode resonators to create a band pass filter with <2dB pass band ripple [32]. In general, supports are placed at the quasi-nodal points to reduce the loss of acoustic energy through the anchors. This can however not be done here since the Lamé mode cannot be excited efficiently by actuation at the corners. With the actuators connected to the resonator at the centre of the side, it will be useful to lump the mass and the stiffness at this point. The effective mass and stiffness seen at this point, can be computed from the mode shape as

$$M_{eff} = \frac{1}{2}\rho t L^2 \tag{2.5a}$$

$$K_{eff} = \frac{1}{2(1+\nu)}\pi^2 Et \tag{2.5b}$$

where ρ is the density, t is the out-of-plane thickness, L is the length of the side, ν is the Poisson's ratio and E is the effective Young's modulus. The resonant frequency of the Lamé mode is [32],

$$\omega_0 = \frac{\pi}{L}\sqrt{\frac{E}{(1+\nu)\rho}} \tag{2.6}$$

Square extensional mode: A resonator vibrating in the square extensional mode undergoes uniform expansion, as shown in Fig. 2-3. This normally causes challenges while designing supports since there are no nodal points that can be utilized. Generally, supports are placed along the corners to deform the mode minimally while utilizing electrostatic transduction based on electrodes placed along the sides [26]. Here the 4 supports that also act as actuators, are placed at the corners. The effective mass and stiffness lumped at the corner of the square extensional mode is given by

$$M_{eff} = \rho t L^2 \tag{2.7a}$$

$$K_{eff} = \pi^2 Et \tag{2.7b}$$

where ρ is the density, t is the out-of-plane thickness, L is the length of the side, and

E is the effective Young's modulus. It can be seen that the ideal square extensional mode parameters, for a free square, are independent of the Poisson's ratio. Based on this, the resonant frequency of the square extensional mode is obtained as

$$\omega_0 = \frac{\pi}{L}\sqrt{\frac{E}{\rho}} \tag{2.8}$$

It is seen that the resonant frequency of the square extensional mode is larger than that of the Lamé mode for a resonator of the same dimensions.

Radial disk mode: The first order mode consists of a disk that expands and contracts radially. An analysis of the set of radial modes was performed by Onoe in 1956 [28]. Radial disk mode resonators have been known to produce high-Q, high frequency devices [33]. These set of modes have a nodal point at the centre and can be efficiently supported at the centre with a stem. Here radial actuators are needed to excite the mode, and a stem alone cannot be used. So radial supports, though undesirable, are utilized here. The resonant frequency of the first radial disk mode for a disk of radius R, is obtained by finding a numerical solution to the equation [28, 33]

$$\frac{J_0\left(\frac{\zeta}{\xi}\right)}{J_1\left(\frac{\zeta}{\xi}\right)} = 1 - \nu \tag{2.9}$$

where

$$\zeta = \omega_0 R \sqrt{\frac{2\rho(1+\nu)}{E}} \tag{2.10}$$

$$\xi = \sqrt{\frac{2}{1-\nu}} \tag{2.11}$$

and $J_i(n)$ is the Bessel function of the first kind of order i. Equations (2.9) - (2.11) can be approximated to a more intuitive form [34]

$$\omega_0 = \frac{(0.342)2\pi}{R}\sqrt{\frac{E}{\rho}} \tag{2.12}$$

The effective mass seen at the perimeter of the disk is given by

$$M_{eff} = \frac{2\pi\rho t}{J_1(hR)^2} \int_0^R r J_1(hr)^2 \, dr. \tag{2.13}$$

where

$$h = \omega_0 \sqrt{\frac{\rho(1-\nu^2)}{E}} \tag{2.14}$$

The value of M_{eff} for the first radial mode, lumped at the edge, is numerically very close to the actual mass of the resonator. The effective stiffness is then obtained from the resonant frequency and the effective mass as

$$K_{eff} = \omega_0^2 M_{eff} \tag{2.15}$$

Disk wineglass mode: The disk wineglass mode has 4 quasi-nodal points along the perimeter and has one node at the center of the disk of radius R. Like the radial disk mode, resonators designed for the wineglass mode can be supported via a central stem, however, fabricating tethers to the quasi-nodes for support is an easier task, and results in higher Q [29]. For the devices that we consider here, the actuators will most likely lie at the anti-node, if the mode is excited. The wineglass mode also provides an option for a differential electrical access, that can be advantageous.

Let the variables ζ, ξ and p be defined as

$$\zeta = \omega_0 R \sqrt{\frac{2\rho(1+\nu)}{E}}, \; \xi = \sqrt{\frac{2}{1-\nu}}, \; p = \frac{\zeta^2}{2(n^2-1)} \tag{2.16}$$

where n is the mode number ($n = 2$ for the disk wineglass mode), and all other variables have the regular meaning. The resonant frequency of this mode can be obtained by numerically solving [28]

$$\left\{ \Gamma_n \left(\frac{\zeta}{\xi} \right) - n - p \right\} (\Gamma_n(\zeta) - n - p) = (np - n)^2 \tag{2.17}$$

32

An approximate solution for the resonant frequency of the disk wineglass mode is [34]

$$\omega_0 = \frac{(0.272)2\pi}{R}\sqrt{\frac{E}{\rho}} \tag{2.18}$$

The radial displacement of the mode, U, and the tangential displacement V, as a function of the radial position r and θ, are given by [28]

$$U = \left\{A\left(\frac{\partial}{\partial r}\right)J_n(hr) + nB\left(\frac{1}{r}\right)J_n(gr)\right\}\cos n\theta \tag{2.19}$$

$$V = -\left\{nA\left(\frac{1}{r}\right)J_n(hr) + B\left(\frac{\partial}{\partial r}\right)J_n(gr)\right\}\sin n\theta \tag{2.20}$$

where h is defined as in eq. (2.14), $\frac{B}{A} = -4.52$, and

$$g = \omega_0\sqrt{2(1+\nu)\frac{\rho}{E}} \tag{2.21}$$

With the displacements known, the lumped mass at the anti-node at the perimeter is obtained by equating the kinetic energies of the total system with that of the lumped system, leading to

$$M_{eff} = \frac{\rho t}{U^2|_{r=R,\ \theta=0}}\int_0^R\int_0^{2\pi}(U^2 + V^2)r\,\mathrm{d}\theta\mathrm{d}r \tag{2.22}$$

The effective stiffness can be obtained from the resonant frequency of the mode and the effective mass using eq. (2.15).

Extensional wineglass ring mode: The first order extension wineglass mode shown in Fig. 2-3 has 4 quasi nodal points at outer and inner surfaces of the ring. The mode also consists of a nodal circle positioned between R_i and R_o. The mode causes two quarters of the ring to expand radially, and the other opposite quarters to be compressed.

The approximate resonant frequency for the first extensional wine glass mode is

$$\omega_0 = \frac{1}{2(R_o - R_i)}\sqrt{\frac{E}{\rho}} \tag{2.23}$$
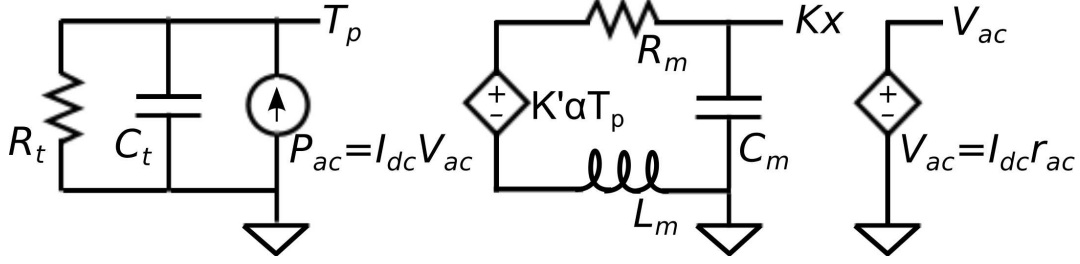
Figure 2-4: Equivalent circuit: Schematic of the thermal, mechanical and piezoresistive loops

The method to numerically obtain the exact frequency is described in detail in Ambati et al. [30]. The expressions for the radial and tangential displacements U and V [31] can be used with eq. (2.22) and (2.15) to obtain the effective mass and stiffness.

2.3 Equivalent Circuit

As mentioned earlier, the oscillator described here consists of the thermal, mechanical and piezoresistive blocks which work in coherence in the device to cause oscillations. The functioning of the device via its various loops is abstracted into an equivalent electrical circuit diagram, to perform an analysis on the nature of contributions of these different factors. The equivalent circuit diagram is shown in Fig. 2-4, and the circuit parameters and their descriptions are listed in table 2.2.

The thermal loop shown in the left side of the equivalent circuit models the temperature of the narrow-beam actuator as function of the power from Joule heating. The actuator is modeled as a rectangular beam of length L as shown in Fig. 2-5. Since we are interested in the sinusoidal variations in the temperature, the ends of the actuators can be modeled as thermal grounds i.e. $T = 0$. Assuming that current flows uniformly across the cross section of the beam, and that conduction is the only mode of heat transfer, the temperature profile is as shown, with a temperature peak $T = T_p$ at the centre of the beam, $x = L/2$.

The equation of steady state heat transfer considering heat conduction with uni-

Variable	Description
R_t	Equivalent thermal resistance $[K/W]$
C_t	Equivalent thermal capacitance $[J/K]$
P_{ac}	Joule heating power $[W]$
T_p	Spatial-peak AC temperature $[K]$
I_{dc}	Constant bias current in the oscillator $[A]$
V_{ac}	AC voltage (oscillator output) $[V]$
K'	Equivalent stiffness of the thermal actuator $[N/m]$
α	Thermal expansion coefficient (length accounted)$[m/K]$
R_m	Lumped equivalent mechanical resistance $[Kg.rad/s]$
C_m	Lumped equivalent mechanical capacitance $[m/N]$
L_m	Lumped equivalent mechanical inductance $[Kg]$
K	Effective stiffness of the resonator $[N/m]$
x	Displacement of the resonator $[m]$
r_{ac}	Resistance variation (AC) due to the piezoresistive effect $[\Omega]$
R_{dc}	Resistance of the structure $[\Omega]$

Table 2.2: Description of the circuit parameters
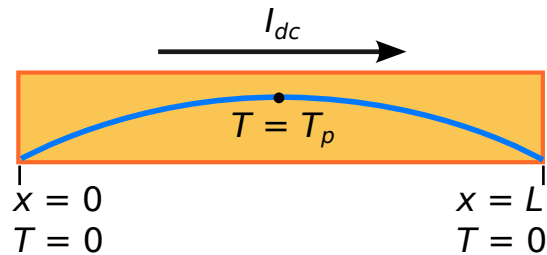
Figure 2-5: Actuator beam with the resulting temperature profile due to Joule heating. The ends of the actuator are assumed to be thermally grounded, and current flow is assumed to cause uniform heat generation.

form heat generation is given by [35],

$$\frac{d^2T}{dx^2} = -\frac{J^2 \rho_e}{k_{th}} \tag{2.24}$$

Using the boundary conditions, $T = 0$ at $x = 0, L$, the temperature profile along the length of the bar is obtained as

$$T = -\frac{J^2 \rho_e}{2k_{th}}x^2 + \frac{J^2 \rho_e}{2k_{th}}Lx = \frac{J^2 \rho_e}{2k_{th}}x(L - x) \tag{2.25}$$

The peak temperature is found at $x = L/2$, and is found to be

$$T_p = \frac{J^2 \rho_e L^2}{8k_{th}} \tag{2.26}$$

and the temperature profile can be rewritten in terms of T_p as

$$T = \frac{4T_p}{L^2}x(L - x) \tag{2.27}$$

The temperature is lumped at the center of the beam so that the nodal voltage of the thermal cycle corresponds to the peak temperature T_p as shown. It is important to be noted that this has to be accounted for in the calculation of K'. Next, the calculated thermal profile is used to obtain the energy stored. The thermal capacitance is obtained by diving the energy stored by the peak temperature.

The total thermal energy stored in the beam is given by

$$\begin{aligned} Q_h &= \int_0^L C_p \rho A T \, dx \\ &= C_p \rho A \frac{4T_p}{L^2} \int_0^L x(L - x) \, dx \\ &= C_p \rho A \frac{2T_p}{3} L \\ Q_h &= C_t T_p \end{aligned} \tag{2.28}$$

where C_p is the specific heat capacity, A is the area of cross section and ρ_m is the

density. The thermal capacitance C_t is obtained as

$$C_t = \frac{2}{3}C_p\rho AL \tag{2.29}$$

The thermal resistance R_t is obtained from Ohm's law,

$$R_t = \frac{T_p}{I^2 R_e} = \frac{L}{8k_{th}A} \tag{2.30}$$

The thermal expasion coefficient $\alpha[m/K]$ can be written as $\alpha_t[1/K] \times L$. K' is calculated by solving the following equation, to account for the varying thermal expansion along the length of the beam.

$$K'\alpha_t T_p L = \int_0^L K_t\alpha_t T \, dx \tag{2.31}$$

This leads to $K' = 2/3K_t$, where K_t is the original stiffness of the bar. This facilitates lumping the temperature at the middle of the bar while reading the displacements and forces at the ends.

The mechanical lumped parameters R_m, C_m and L_m are dependent on the mode shape and known for common resonant modes. The standard equation of motion of a damped single degree-of-freedom (1DOF) system is $m\ddot{x} + b\dot{x} + kx = F$, which can be rewritten as

$$\ddot{x} + \frac{\omega_0}{Q}\dot{x} + \omega_0^2 x = \frac{F}{m} \tag{2.32}$$

Here the forcing function F is due to the thermal expansion force of the actuator, and is given by

$$F = K'\alpha T_p = K'\alpha I_{dc}^2 r_{ac}\left(R_t \parallel \frac{1}{j\omega C_t}\right) \tag{2.33}$$

where

$$r_{ac} = \frac{x}{L}E\pi_l R_{dc} = K_{pr}xR_{dc} \tag{2.34a}$$

$$K_{pr} = \frac{E\pi_l}{L} \tag{2.34b}$$

Substituting equations (2.33) and (2.34a) in the equation of motion, and assuming

$x = x_0 e^{-j\omega t}$, the imaginary terms can be equated to 0 for sustained oscillations, as the effective damping is 0 in this state. This leads to

$$\omega \frac{\omega_0}{Q} = K'\alpha I_{th}^2 K_{pr} R_{dc} \left(\frac{\omega C_t R_t^2}{1 + (\omega R_t C_t)^2} \right) \frac{1}{m} \tag{2.35}$$

Solving for the threshold current in the above equation gives

$$I_{th}^2 = m \frac{\omega_0}{Q} \frac{1 + (\omega R_t C_t)^2}{K'\alpha K_{pr} R_{dc} C_t R_t^2} \tag{2.36}$$

To calculate the final oscillator frequency, we look at the phase difference for the individual elements of the oscillator as shown in Fig. 2-2. For sustained oscillations, the total delay through the entire loop has to be an integral multiple of 2π. This necessitates that

$$\phi_T + \phi_M = tan^{-1}\left(-\frac{\omega}{Q}\frac{\omega_0}{\omega_0^2 - \omega^2} \right) + tan^{-1}(-\omega\tau_T) = (2n-1)\pi, \, n \in Z \tag{2.37}$$

$$\implies tan^{-1}\left(-\frac{\omega\omega_0 + \omega\tau_T Q(\omega_0^2 - \omega^2)}{Q(\omega_0^2 - \omega^2) - \omega^2\omega_0\tau_T} \right) = (2n-1)\pi \tag{2.38}$$

$$\implies \omega\omega_0 + \omega\tau_T Q(\omega_0^2 - \omega^2) = 0 \tag{2.39}$$

Therefore, the frequency of oscillations is given by

$$\omega = \omega_0 \sqrt{1 + \frac{1}{\omega_0 \tau_T Q}} = \omega_0 \sqrt{1 + \frac{\tau_M}{\tau_T Q}} \tag{2.40}$$

where $\tau_T = R_t C_t$ is the thermal time constant, and τ_M represents the mechanical time constant and is equal to $1/\omega_0$. Equation (2.40) shows that the final oscillation frequency ω is much closer to the resonant frequency of the resonator ω_0 with a higher Q. Substituting this in the threshold current equation (2.36), we get,

$$I_{th}^2 = \frac{m}{Q\tau_M} \left\{ 1 + \frac{\tau_T}{\tau_M Q} + \left(\frac{\tau_T}{\tau_M} \right)^2 \right\} \frac{1}{K'\alpha K_{pr} R_{dc} R_t \tau_T} \tag{2.41}$$

Results from (2.40) and (2.41) indicate that both the oscillation frequency and the

38

threshold current density, two key metrics, are dependent on the quality factor, and more importantly, on the ratio of the thermal and mechanical times constant. By changing the length of the actuator and the dimension of the resonator, both the time constants can be controlled. The set of devices fabricated in this work will span a wide range of these two time constants.

2.4   Scaling Trends

In order to find the optimal values for dimensions, and the general effects of scaling, let us adopt the following generalizations:

The effective mass can be written as a coefficient x_{EM} times the actual mass,

$$m = M_{eff} = x_{EM}\rho_M D_M^2 T_M \tag{2.42}$$

where D_M and T_M are the dominant planar dimension and the thickness. For e.g., D_M would be the side of the square extensional mode resonator and the radius in a radial disk resonator. Subscripts M and T denote that they are mechanical and thermal parameters respectively. Some earlier results can now be updated as shown below.

$$\tau_M = \frac{1}{\omega_0} = \frac{D_M}{\beta_{mode}}\sqrt{\frac{\rho_M}{E}} \tag{2.43a}$$

$$R_t = \frac{L_T}{8k_{th}A_T} \tag{2.43b}$$

$$C_t = \frac{2}{3}C_p\rho_M A_T L_T \tag{2.43c}$$

$$\tau_T = \frac{C_p\rho_M L_T^2}{12k_{th}} \tag{2.43d}$$

$$K' = \frac{2EA_T}{3L_T} \tag{2.43e}$$

$$\alpha = \alpha_t L_T \tag{2.43f}$$

$$K_{pr} = \frac{E\pi_l}{L_T} \tag{2.43g}$$

$$R_{dc} = \frac{n_{el}L_T}{\sigma_e A_T} \tag{2.43h}$$

$$\frac{\tau_T}{\tau_M} = \frac{C_p \beta_{mode}\sqrt{E\rho_M}}{12 k_{th}} \frac{L_T^2}{D_M} \tag{2.43i}$$

where n_{el} is the effective number of actuators in series in the current path, σ_e is the electrical conductivity, and β_{mode} is some mode dependent factor, that satisfies eq. (2.43a) and relates D_M, E, and ρ_M with the resonant frequency .

Substituting (2.43) into the current equation (2.41), the threshold current density J_{th} is now obtained as

$$J_{th}^2 = \chi\frac{T_M}{A_T\sqrt{D_M}}\left\{\left(\frac{\tau_M}{\tau_T}\right)^{1.5} + \frac{1}{Q}\left(\frac{\tau_M}{\tau_T}\right)^{0.5} + \left(\frac{\tau_M}{\tau_T}\right)^{-0.5}\right\} \tag{2.44}$$

where

$$\chi = 2\sqrt{3}\frac{x_{EM}\sigma_e\rho_M^{0.25}k_{th}^{0.5}C_p^{0.5}\beta_{mode}^{2.5}E^{-0.75}}{Q\alpha_t\pi_l n_{el}} \tag{2.45}$$

The thermal and mechanical time constants have no dependence on T_M and A_T. From (2.44), it is seen that it is favorable to minimize $\frac{T_M}{A_T}$ to reduce the threshold current density. This indicates that $\frac{A_T}{T_M}$ which is the width of the actuating narrow beam, can be maximized since the thickness of the actuator and the resonator proof mass are identical, and denoted by T_M.

The frequency of interest is tailored for the chosen oscillator design by picking the prominent dimension D_M based on (2.43a). The optimal ratio of the time constants, for minimizing the threshold current density is obtained as

$$\left(\frac{\tau_M}{\tau_T}\right)_{opt} = \sqrt{\left(\frac{1}{6Q}\right)^2 + \frac{1}{3} - \frac{1}{6Q}} \approx \frac{1}{\sqrt{3}} \tag{2.46}$$

Substituting this result in (2.44), we get the minimum threshold current density to be

$$J_{th}^2|_{min} \approx 1.75\chi\frac{T_M}{A_T\sqrt{D_M}} \tag{2.47}$$

There is particular interest in understanding how the threshold current density scales with the frequency. From (2.47) it is seen that the threshold current density reduces

40

with increase in the characteristic mechanical dimension D_M, with the following relationship.

$$J_{th} \propto \frac{1}{D_M^{0.25}} \propto \omega_0^{0.25} \tag{2.48}$$

As we operate at higher frequencies, and the dimensions shrink, the minimum threshold current density increases, though sublinearly.

Chapter 3

Fabrication

Different thermally-actuated piezoresistively-sensed silicon oscillators described in the previous chapter were fabricated at the Microsystems Technology Laboratories (MTL) cleanroom at MIT, and the release step was performed at the Nanostructures laboratory(NSL). The process is carried out on an SOI wafer, and uses 3 masks. All the devices are integrated on single die of size $1.2cm \times 1.2cm$, shown in Fig. 3-1, and each wafer holds 36 identical dies.

3.1 Process Details

The various process specifications and requirements are described in detail in this section. The complete fabrication sequence and schematics are in Sec. 3.2.

3.1.1 Wafer

The n-type (Sb, 0.01 - 0.02 Ωcm, 2.2 μm thick device layer) SOI wafers used in this work were customized and acquired from Ultrasil Corporation. The buried oxide (BOX) is 2.1 μm thick. Based on the requirements on the uniformity and quality of the device layer etch, the desired device layer thickness is estimated to be 1.5 μm. So the fabrication process starts with wafer thinning steps to reduce the device layer thickness by 0.7 μm. The new wafer is RCA cleaned following the standard process:
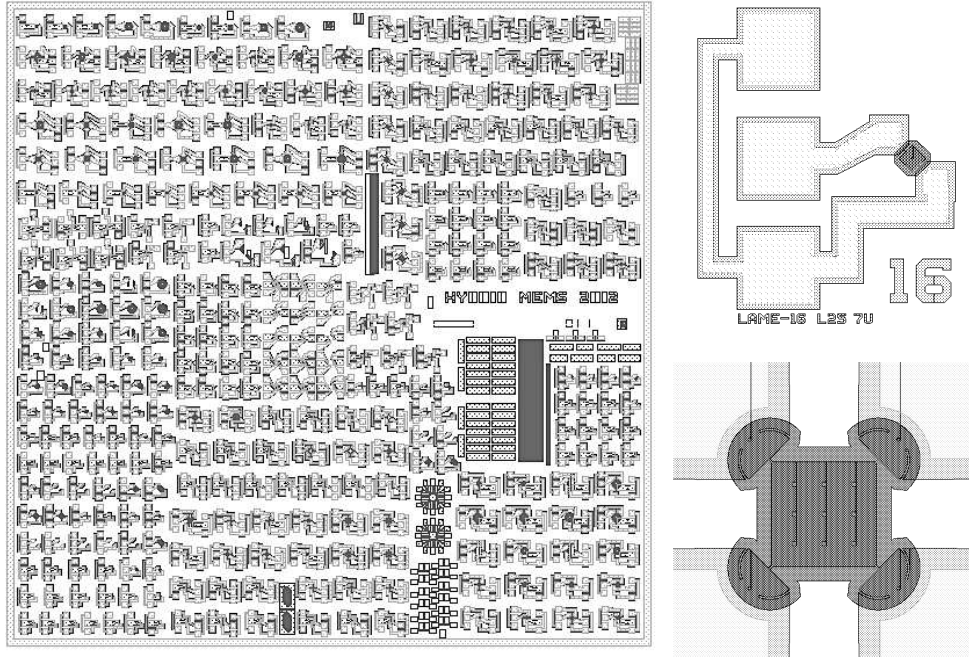
Figure 3-1: (Clockwise from left) Snapshot of the full die layout, a single 2-support Lamé mode device showing the GSG pad and electrical routing to device, and a closeup of a 4-support square extensional mode device showing release holes and reflectors at the anchors.

SC1 (5:1:1 DI water : NH_4OH : H_2O_2) for 10 mins at 80°C, followed by a 1 minute dip into a 1:50 solution of HF, and then followed by SC-2 (6:1:1 DI water : HCl : H_2O_2) for 15 mins at 80 °C. After the RCA clean, the wafer was wet oxidized (in the presence of H_2 and O_2) at 1050°C for 3 hrs 20 mins in a furnace specially used for thick oxide formation. The oxide thickness measurements were performed on the monitor wafers using ellipsometry, and were found to be 1.02 μm. The wet oxide formed was removed using a buffered oxide etch (BOE) in an acid hood for 17 mins. The etching rate was found to be a little slower that usual in this case, since the same solution may have been used several times earlier. To bring down the device layer thickness to desired value, this whole cycle is effectively repeated with slight changes. After the RCA clean, the wafer is now wet oxidized at 1000°C for 2 hrs 15 mins. This oxide, estimated to be 0.6 μm thick, is also removed with BOE. After removing 1.6 μm of thermal oxide, the device layer is about 1.5 μm thick, the required thickness.

3.1.2 Silicon Etch

To transfer the device pattern on to the silicon device layer, a resist mask is used. The wafer after being thinned down to the required thickness, is coated with a positve resist (SPR 700) using a coater at 4000 rpm, after a coat of HMDS, an adhesion promoter. The resulting resist thickness is 900 nm. Photolithography is performed using a Nikon Stepper, to transfer the device layer pattern from the mask on to resist. The 6-*inch* wafer is exposed with 36 device dies shown in Fig. 3-1. To reduce recurrent alignment problems, the rest of the wafer was left empty, except for the additional 12 alignment dies that only contain the alignment marks required for aligning the future levels. The exposure was set to 140 ms per die with a 0.4 μm focus offset to get the best resolution. The exposed resist is developed using the MF-CD 26 developer using a spray puddle technique on a track for 60 s. The developer process also includes a post exposure bake to enhance the resist contrast.

The pattern on the resist is etched into the device layer using STS-2, a Deep Reactive Ion Etch (DRIE) tool (ST Systems Multiplex ICP). The DRIE tool was used with a modified process compared to the usual DRIE process where there are cycles of etching (SF_6) followed by passivation cycles (C_4F_8). The process utilized here is carried out in the presence of both the etching and passivation gases at the same time. The inductively coupled plasma (ICP) etch process is performed at a pressure of 22 mTorr with 40 sccm SF_6 and 80 sccm C_4F_8, and with 100 W platten power and 600 W coil power for 6 mins. The exposed parts of the device layer are etched away until the BOX is reached. This can be visually confirmed when the shiny device layer parts are etched away, revealing the dull BOX parts in the exposed regions. The results of the optimized etch recipe on bulk silicon samples and the SOI wafer are shown in Fig. 3-2. With a well executed photolithography process, 0.5 μm features can be etched to a depth of 1.5 μm with no distortions along the etch depth as shown. The process also prevents the formation of any scalloping, characteristic of any DRIE process, and results in smooth and straight side walls. The process also allows for the formation of 0.9 μm wide steps and trenches with minimal rounding,
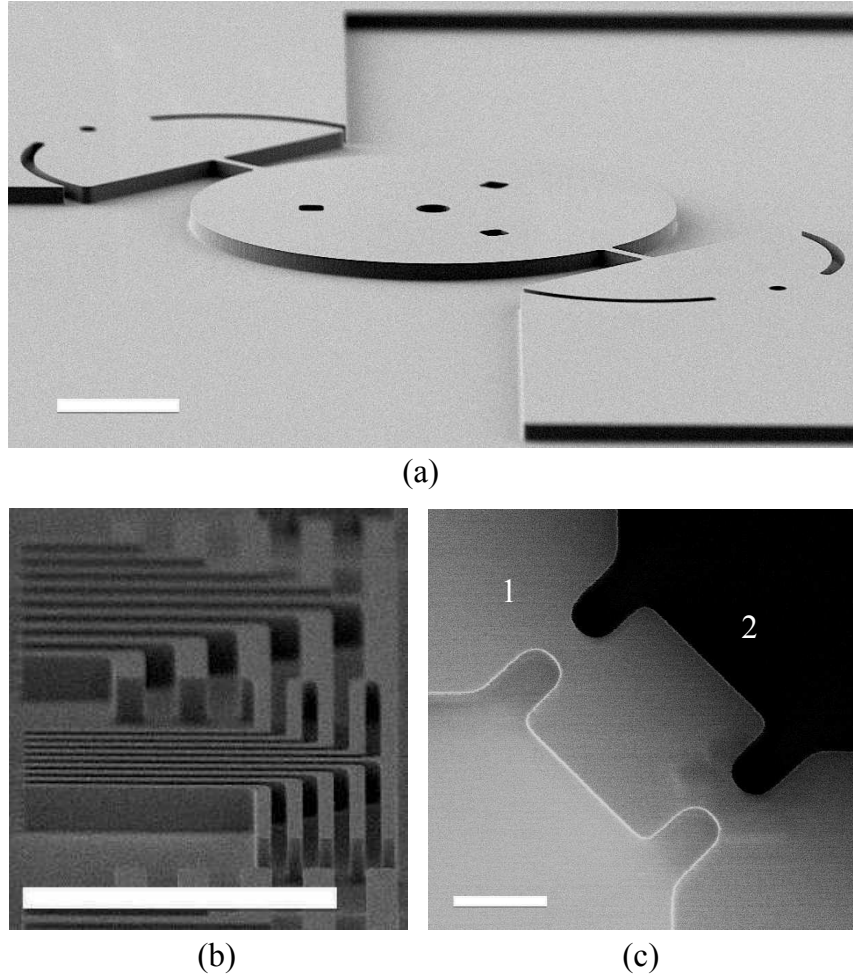
Figure 3-2: (a) Tilted view SEM image of the optimized 2 μm deep silicon etch, performed on a device pattern on a bulk Si wafer (scale bar: 10 μm) (b) Tilted view of a 0.5 μm pattern on the bottom right (scale bar: 10 μm) (c) Top view of 2-support Lamé mode device etched on an SOI wafer. Region 1 is the silicon device layer and region 2 is the exposed BOX (scale bar: 2 μm)

which is required for the 2-support Lamé mode device shown in Fig. 3-2c. After the etching is completed, the resist is removed by ashing in an O_2 plasma. The alignment dies described earlier are also etched onto the device layer now, and consist of 4 individual alignment marks used for x and y, global and fine alignment. An alignment mark consists of a 2D-array of square pillars or trenches (typically about 4 μm in size). A sample alignment mark is shown in Fig. 3-3.
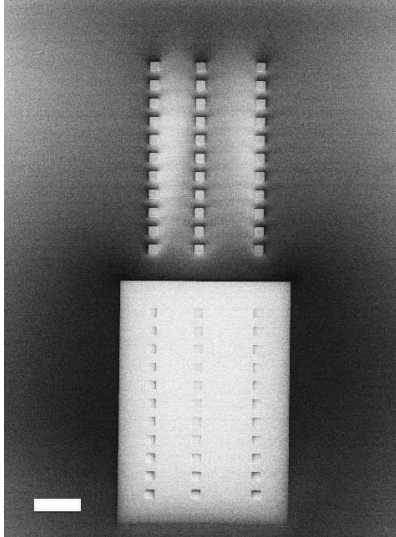
Figure 3-3: Alignment marks etched on to the device layer of the SOI wafer for use by the Nikon Stepper for aligning subsequent levels. Alignment pattern consists of an array of 4 $\mu m \times 4$ μm squares (scale bar: 20 μm).

3.1.3 Geometry Factors

With the completion of the device layer etch, a major part of the basic device geometry is formed. We'll now discuss details of extra processes used to enhance device performance and make the overall fabrication process robust.

Looking ahead at the last step of the fabrication process, which is the final release step, based on the current geometry, a part of the resist used to cover regions outside the release window, would rest on the BOX. When the BOX is removed by the buffered oxide etch during release, the part of the resist originally resting on the BOX is left hanging and has a large tendency to peel. This can be avoided by removing the BOX from such regions so that the resist mask during release rests on either the device layer or on the handle wafer, both of which remain intact during the release step. This can be done easily by using the device layer as an etch mask for the underlying BOX. This step will expose the device layer to the gases used to etch the BOX though, and cause surface roughness that is detrimental to the device performance. To avoid this, the release window mask is inverted using an image reversal resist to remove the exposed BOX that would come in contact with the resist mask during release. This also protects the crucial part of the device layer from the gases used for dry etching

47

BOX. This can be seen in the fabrication process schematics in section 3.2. Another important factor is that both the BOX dry etch and the previous device layer etch, tend to leave a teflon-like polymer on the exposed regions and cause some amount of roughness. This can be mitigated by performing a wet oxidation and strip step that removes the polymer and reduces the roughness. This should yield devices with better quality factors. These two steps are described below.

To invert the release window mask, image reversal resist AZ5214 is used. The wafer is coated with AZ5214 at 2500 rpm for 30 s, and soft-baked at 95°C for 30 s. This creates a resist that is 2 μm thick. The release window pattern is now exposed using the stepper on all the device dies for 60 ms each. Then the image reversal bake is performed at 120°C for 120 s. To complete the image reversal procedure, flood exposure is performed on each of the dies for 400 ms. The resist is now developed using AZ422 MIF developer for 3 mins 30 s. The resist is then hard baked at 120°C for 120 s to be effective as an etch mask, and loaded into an ICP oxide etcher (AME 5000 from Applied Materials). The oxide etch is performed after a 30s long O_2 descum to get best results. The oxide etch is done at 600 W power for a total of 800 s with breaks for cooling, in the presence of 50 sccm CHF_3, 10 sccm CH_4, and 100 sccm Ar. This ensures that the exposed BOX is removed, with the exact endpoint monitored using an endpoint controller. The resist mask is now cleared using a standard Piranha clean (3:1 concentrated H_2SO_4 to H_2O_2). Figure 3-4 shows scanning electron microscope (SEM) images of a 4-support ring device, and 4-support square extensional mode oscillator at this stage of the fabrication process. The different regions in the images are described in the caption. The sharp contrast between the exposed and covered device layer regions (1 & 2) comes from two factors. First, the oxide etch has a selectivity of around 20:1 (oxide to silicon) for the chemistry used and the current fill factor. So there is a small height difference between the exposed and unexposed regions of the device layer. Secondly, the exposed regions are covered by polymers formed during the etching process.

Prior to performing wet oxidation, the wafer is RCA cleaned. The wafer is then loaded in a wet oxidation furnace where oxidation is performed at 850°C in the pres-
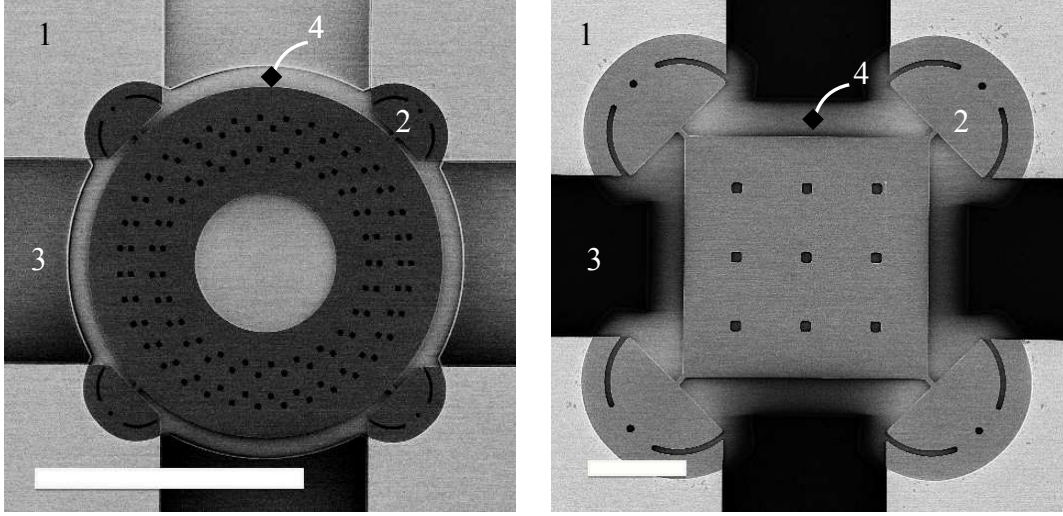
Figure 3-4: (Left) Top view of the device after the completion of the Si device layer and BOX etches. After the device layer etch, the 2 μm BOX etch is performed to expose the handle wafer using the inverted release window. Regions 1 and 2 shows parts of the device layer that were exposed, and protected during this etch. The etch chemistry leaves a coat of polymers on the exposed region causing a sharp contrast between regions 1 and 2. Region 3 is the exposed silicon handle wafer, and region 4 is the BOX that was protected by the resist mask. Scale bars: 100 μm (left), 20 μm (right).

ence of H_2 and O_2 gases for 32 mins. This leads to the formation of about 39 nm of oxide which is stripped away using a 1 minute dip in BOE, which includes a significant over-etch duration [36].

3.1.4   Metals and Contact Properties

Forming metal contacts and releasing the devices are the two remaining steps at this stage. To form an ohmic contact, required for reducing the voltage drop at the junction, and allowing large current densities, the contact formation process involves degenerately doping the contact, forming a nickel silicide and depositing a Ti/Al metal stack.

To raise the local donor concentration at the contacts from 10^{18} cm^{-3} to over 10^{20} cm^{-3}, phosphorous ions are implanted into the contact region. To form the implantation mask, AZ5214 (image reversal resist) is coated on the wafer at 2500 rpm for 30 s after a coat of HMDS. After soft-baking the resist at 95°C for 30 s, the

metal layer mask is used to expose the pattern on the coated wafer for 60 ms per die using the Nikon Stepper. The image reversal bake is then performed at 120°C for 120 s. After the completion of a flood exposure process on each die for 400 ms using the Nikon Stepper, the resist is developed for 3 mins 30 s using AZ 422 MIF developer. The resist pattern has open windows in the regions where metals will be deposited, and these are also the regions that need doping to enhance the local donor concentration. The wafer is sent to Innovion Corporation for ion implantation. Phosphorous ions are implanted at an energy of 14 keV, with a total dose of $2.5 \times 10^{15}/cm^2$. Once implantation is completed, the resist is stripped, and the wafer is cleaned with a double Piranha clean. After performing an RCA clean, the wafer is loaded into a furnace for the activation anneal. The activation anneal is performed at a peak temperature of 850°C for 10 minutes. The wafers are loaded at a temperature of 600°C and the entire process including the ramp up and ramp down times lasts 60 mins. Once this step is completed, the final surface donor concentration in the contact regions is $> 10^{20}/cm^3$. To ensure the concentration at the surface is high after the annealing process, the implantation and annealing processes were simulated using Sentaurus Process. The annealing temperature was set to 850°C uniformly for 60 mins in the simulations to get conservative results. It can be seen from Fig. 3-5 that the donor concentration at the surface is still above $10^{20}/cm^3$.

To improve the contact properties further, a process to form nickel-silicide at the contact is performed. The image reversal resist process described above, for forming the doping mask is repeated. This resist pattern has open windows at the metal contact regions. The wafer is dipped in a 1:50 solution of HF to remove the native oxide from the open regions and immediately loaded into the e-beam evaporator where 40 nm of Ni is deposited. A liftoff process is performed in acetone to remove the Ni deposited on top of the resist. The wafer is rinsed in iso-propanol(IPA) and blown dry with N_2. This leaves Ni only in the contact regions. To form a silicide, the wafer is rapid thermal annealed at 500°C for 30 s. A part of the 40 nm thick nickel at the interface with silicon is consumed to form the nickel silicide. The remaining unconsumed Ni, which lacks good electrical conductivity, is removed in a Piranha
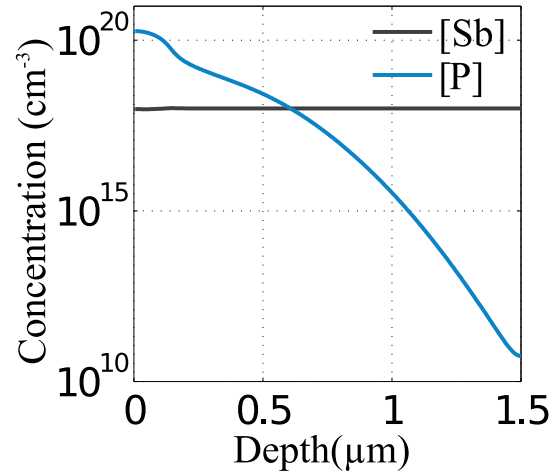
Figure 3-5: Simulated profile of the active phosphorous concentration after implantation at 14 keV with a $2.5 \times 10^{15}/cm^2$ dose, followed by an activation anneal at 850°C for 60 mins. The base antimony concentration is also shown after the annealing process. Simulation was performed using Sentaurus Process.
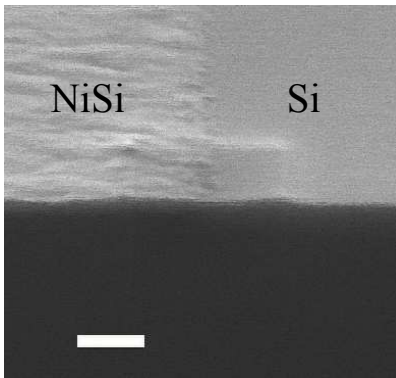
Figure 3-6: Cross-section image of a silicon wafer showing regions with nickel silicide (scale bar : 200 nm)

solution. A cross section SEM image of the nickel silicide process performed on a sample bulk silicon wafer is shown in Fig. 3-6. The region with the silicide can be easily distinguished from the bare silicon regions and show surface roughness.

The image reversal resist process is repeated again to open windows at regions where metal is to be deposited. AZ5214 is coated on the wafer at 1000 rpm for 30 s and soft-baked as described earlier. The pattern exposure (70 ms/die), image reversal bake and flood exposure (450 ms/die) steps are repeated as described earlier. After developing in the AZ 422 MIF developer solution for 3 mins 30 s, the wafer is dipped in 1:50 diluted HF solution to clear any native oxide at the contact regions. Finally

51
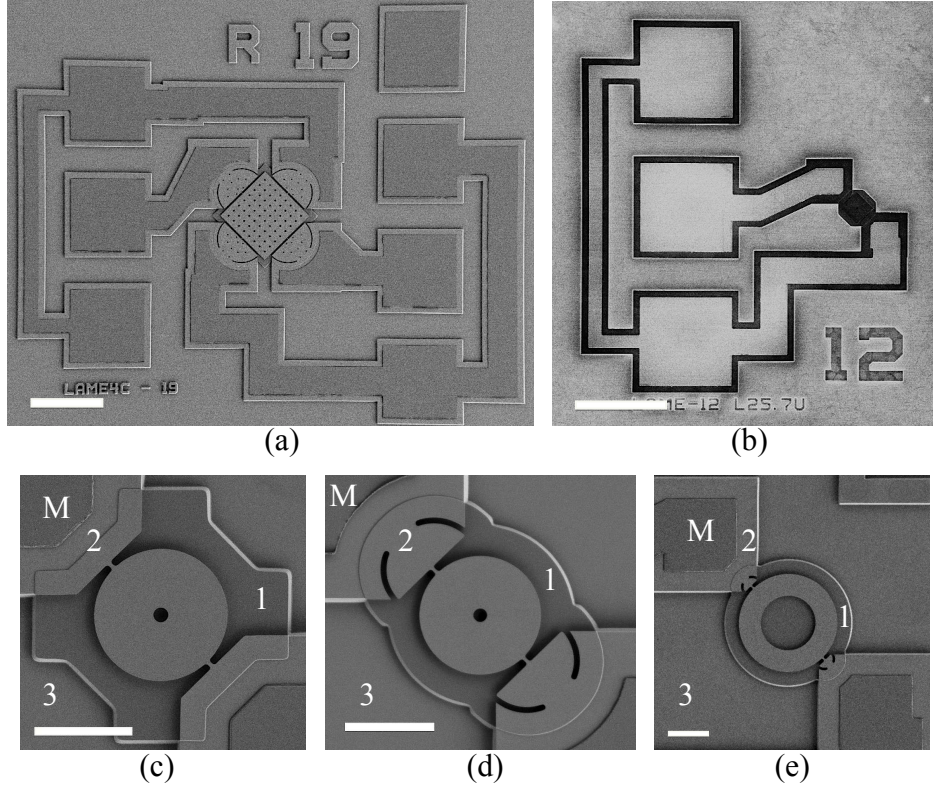
Figure 3-7: (a) and (b) show images of the complete 4-support and 2-support devices after metal deposition and liftoff (scale bars: 100 μm). (c), (d) and (e) show close zoomed views of a disk oscillator, a disk oscillator with reflective anchors, and a mechanical ring oscillator. Regions 1, 2, 3 and M correspond to the BOX, silicon device layer, exposed handle wafer and the Ti-Al metal contacts respectively (scale bars: 20 μm).

50 nm of Ti followed by 500 nm of Al are deposited in the e-beam evaporator. Liftoff is performed overnight in acetone, occasionally degassing to enhance the liftoff speed. The wafer is cleaned repeatedly in IPA and blown dry using a N_2 gun. Figure 3-7 shows SEM images of various devices after metal liftoff. The metal regions are marked 'M' in figures (c)-(e).

3.1.5 Release and Drying

Finally, to make the oscillators functional, the moving parts of the device are released and suspended. To achieve this, the BOX where the devices are currently resting on, is etched away using BOE. Since metals are etched by various acids including HF, which is a constituent of BOE, release is performed in select windows while protecting

<table>
<tr><td>(a)</td><td>(b)</td><td>(c)</td></tr>
</table>
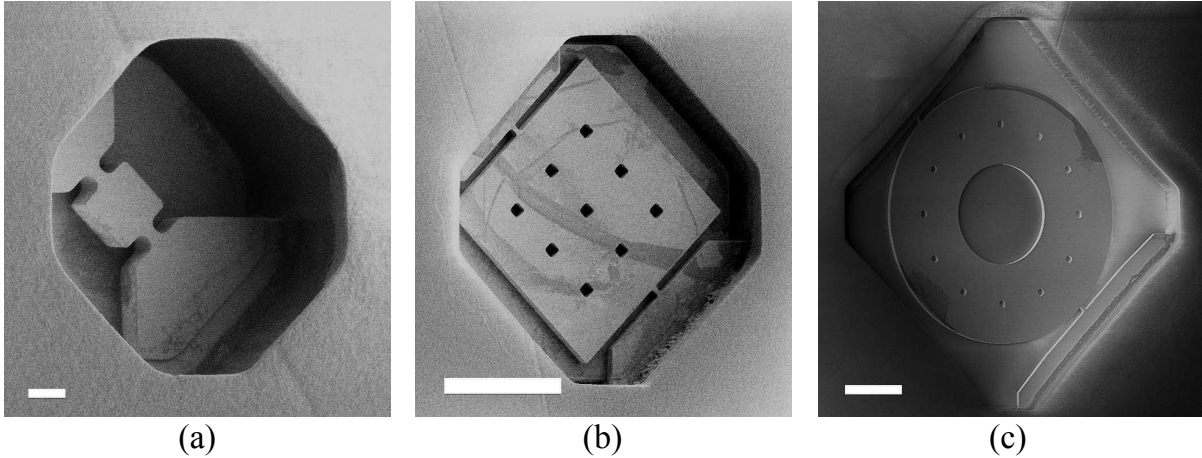
Figure 3-8: Devices prior to release: The images show devices in the release windows formed with 10 μm thick resist. The regions outside the devices inside the release window show the BOX. (a) and (b) show a 2-support Lamé mode device, and (c) shows a 2-support ring oscillator (scale bars: a - 2 μm, b & c - 20 μm).

the metal contacts with resist. The release windows or openings in the resist, provide access for BOE to reach and remove the buried oxide. Once the buried oxide is etched and the devices are released, the dies are carefully dried using a critical point dryer to ensure that the liquid meniscus does not collapse the device permanently. Since the release and drying processes are more likely to fail and affect the yield drastically, the wafer is cleaved into dies before proceeding once release windows are opened.

To create the release windows, a thick resist (AZ4620) is coated on the wafer at 3000 rpm for 40 s, and soft-baked at 95°C for 30 s. The pattern from the release window mask is exposed using the Nikon Stepper for 200 ms per die. The resist is developed in a solution of 1:1 AZ405 to DI water for 20 s initially, and then carefully for a few extra seconds looking at the wafer repeatedly to check the state of development. The wafer is then cleaved by hand using a diamond scribe to isolate individual dies. Figure 3-8 shows a set of SEM images of 2-support devices inside the release window.

Prior to release, the die is hard-baked at 100°C for 3-5 mins to harden the resist, and prevent peeling. After a gradual cool down, the die is placed in a DI water solution in an ultrasonication bath. Ultrasonication and degassing helps the liquid reach the small crevices and remove bubbles. The die is removed carefully and transferred into the BOE solution. Based on the design, release holes were placed on devices such that

(a)   (b)
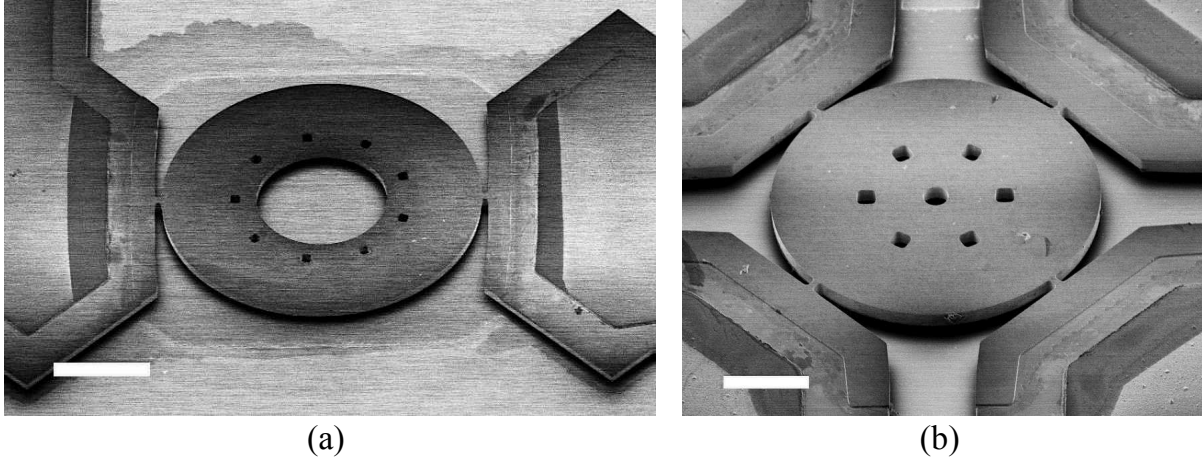
Figure 3-9: Released devices: (a) 2-support ring oscillator (b) 4-support disk oscillator. The boundary of the release window where BOX was etched is visible (scale bars: a - 20 μm, b - 10 μm).

the undercut required to remove all the underlying BOX is less than 10 μm. For this, the die is left inside the BOE solution for 105-110 mins, with occasional degassing to help remove any new bubbles that may be formed within the release window. The device is repeatedly rinsed in water, and in acetone to remove the resist, while making sure that the devices never see the liquid meniscus. The device is carefully rinsed in IPA and transferred to an ethanol bottle carefully. Critical point drying (CPD) is performed in CO_2 using the Tousimis critical point dryer station. CPD ensures that the liquid to gas phase transformation occurs without crossing a phase boundary, instead via a transition through the supercritical region. After CPD or super critical drying is completed, the device is carefully removed and sintered in a furnace in the presence of forming gas (N_2:H_2 12.5:1) at 460°for 30 mins, to improve the electrical properties of the device, to conclude the fabrication process. Figure 3-9 shows SEM images of the final released devices where the region exposed to BOE is visible.

3.2   Process Flow and Schematic

A schematic of the cross section of key steps during the fabrication is shown Fig. 3-10 and the complete step by step process flow is listed in table 3.1.

(a) Step: 7

(b) Step: 12

(c) Step: 15

(d) Step: 17

(e) Step: 24

(f) Step: 39

(g) Step: 43

(h) Step: 46

Silicon ■ BOX ■ PR ■ Titanium ■ Aluminum
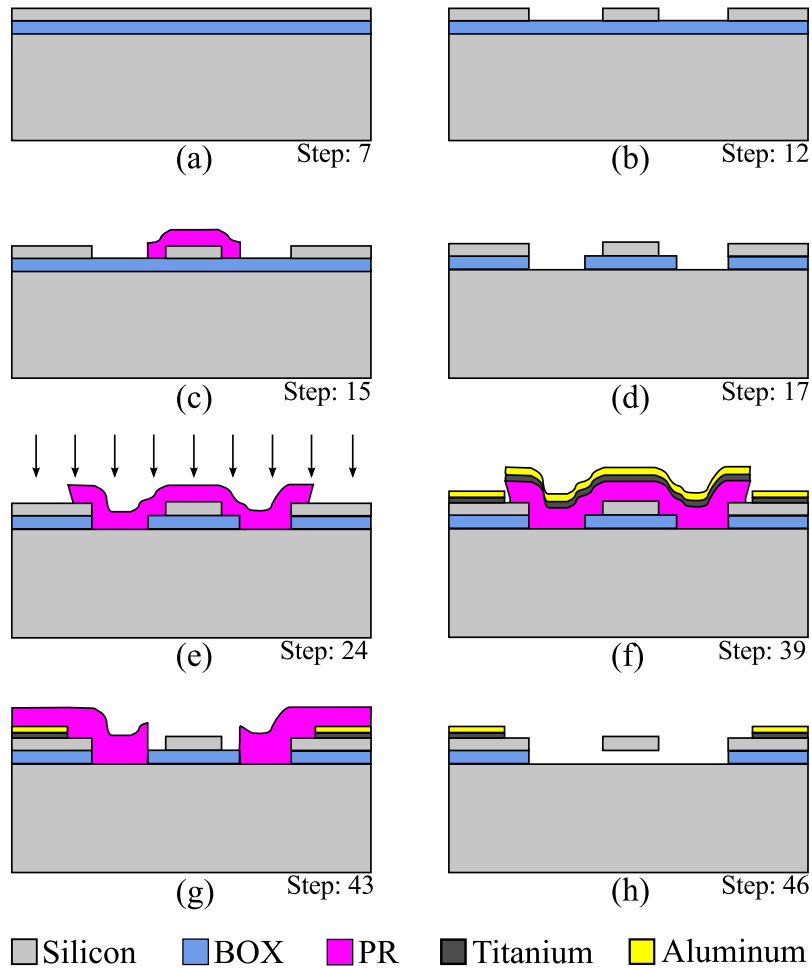
Figure 3-10: Fabrication process flow: (a) SOI wafer after device layer thinning (b) Patterned device layer (c) Inverted release window mask for BOX etch (d) After BOX etch (e) Phosphorous ion implantation (f) Evaporation of metal stack (Ti/Al) after siliciding (g) Patterned release window in thick resist (h) Final released device. (Corresponding step number in the process sequence 3.1 is indicated in the bottom right of each schematic)

Step	Description	Machine
1	Starting material: 6-*inch* SOI wafer (2-2.2 μm device layer, 2 μm BOX)	
2	RCA Clean	RCA - ICL
3	Wet oxidation (1 μm oxide) for wafer thinning	Tube5D-Thickox- ICL
4	Buffered oxide etch (BOE) to remove the oxide	OxEtch BOE - ICL
5	RCA Clean	RCA - ICL
6	Wet oxidation (0.6 μm oxide) for wafer thinning	Tube5D-Thickox- ICL
7 (a)	BOE to remove the oxide	OxEtch BOE - ICL
8	Spin photoresist (PR) (1 μm to etch 1.5 μm of Si)	Coater6 - ICL
9	Photolithography with the device layer mask	i-Stepper
10	Develop PR	Coater6 - ICL
11	Etch the pattern into the silicon device layer (etch 1.5 μm Si)	STS2 - TRL
12 (b)	Strip resist	Asher - ICL
13	Spin PR (2 μm of image rev. res.)	Coater - TRL
14	Photolithography with release window mask (bake, flood exp for image reversal)	i-Stepper
15 (c)	Develop PR	Photo wet - TRL
16	Etch oxide (BOX of SOI wafer)	AME 5000 - ICL
17 (d)	Piranha clean to strip resist	Acidhood - TRL
18	RCA clean	RCA - TRL
19	Wet oxidation 850°C (immediately after the previous step)	TubeA2-WetOxBond - TRL
20	Buffered oxide etch (timed)	Acidhood - TRL
21*	Spin PR (Image Rev. Res.)	Coater - TRL

22*	Photolithography with metal layer mask (bake, flood exp for Image reversal)	i-Stepper
23*	Develop PR	Photo wet - TRL
24* (e)	Ion implantation to form ohmic contacts (Phosphorous, 14 keV, $2.5e15/cm^2$)	Innovion Corp.
25*	Strip resist	Asher - TRL
26*	Double Piranha clean	Acid Hood - TRL
27*	RCA clean	RCA - TRL
28*	Dopant activation (800-950°C)	TubeA2-WetOxBond - TRL
29	Spin PR (Image rev. res.)	Coater - TRL
30	Photolithography with the metal layer mask (bake, flood exp for Image reversal)	i-Stepper
31	Develop PR	Photo wet - TRL
32	Deposit 40 nm Ni	ebeamCMOS - ICL
33	Liftoff the evaporated metal in acetone, IPA	Photo wet -TRL
34	Rapid thermal anneal(RTA) at 500°, 30 s (to form silicide)	RTA2 ICL
35	Piranha clean (to remove Ni not consumed)	Acidhood - TRL
36	Spin PR (2 μm or thicker, Image Rev. Res.)	Coater - TRL
37	Photolithography with metal layer mask(bake, flood exp for Image reversal resist)	i-Stepper
38	Develop PR	Wet - TRL
39 (f)	Evaporate 50 nm Ti and 500 nm Al	eBeamAu - TRL
40	Liftoff the evaporated metal in Acetone, IPA	Photo wet - TRL
41	Spin PR (6 μm or thicker)	Coater - TRL
42	Photolithography with release window mask	i-Stepper
43 (g)	Develop PR	Coater - TRL

44	Dice into chips	Cleave by hand
45	Release devices with BOE and remove resist	Acidhood $\rightarrow$ Photowet - TRL
46 (h)	Critical Point Drying (CPD) in CO_2	CPD - NSL
47	Sintering	TubeB1Au - TRL

Table 3.1: Stepwise fabrication process. Corresponding schematics in Fig. 3-10 are indicated in brackets alongside the step number. Steps marked with '*' are required to locally dope the silicon contact surface. The first run of the process did not include these steps.

Chapter 4

Results: Calculations and Experimental Results

4.1 Analytical Calculations

Exploring the upper limits of frequencies attainable with these oscillators, and reducing the threshold current densities is one of the main goals here. The ratio of the mechanical and thermal time constants was found to be an important factor for improving the efficiency of actuation based on earlier analysis. This result was obtained assuming a constant Q, independent of the actuator length. To verify these results, devices operating at a wide range of frequencies, and thermal time constants are required. Devices meeting these requirements were designed using the equations from chapter 2.

Using 4-point probe measurements, the resistivity of the device layer was measured to be 0.0198Ω cm closer to upper limit of the $0.01 - 0.02$ Ωcm range specified by the manufacturer. Table 4.1 lists the values of various parameters used in calculations. Bulk silicon values are used for most properties. The longitudinal piezoresistive coefficient along the $<100>$ direction is used as all actuators are aligned 45°with respect to the primary flat of the (100) n-type silicon wafer. The thickness of the device layer is assumed to be 1.5 μm for calculations, however, the variation in the device thickness is $\pm 0.5\mu m$.

Parameter	Description	Value
C_p	Specific heat capacity	$702\ J/Kg - K$
E	Young's modulus	$180\ GPa$
k_{th}	Thermal conductivity	$113\ W/m - K$
Q	Quality factor	10^4
t, T_M	Thickness	$1.5\ \mu m$
α_t	Normalized thermal expansion coefficient	$2.6 \times 10^{-6}\ K^{-1}$
ν	Poisson's ratio	0.28
π_l	Longitudinal piezoresistive coefficient	$-102.2 \times 10^{-11}\ Pa^{-1}$
ρ, ρ_M	Density	$2330\ Kg/m^3$
ρ_e	Electrical resistivity	$0.02\ \Omega\ cm$
σ_e	Electrical conductivity	$5 \times 10^3\ \mho/m$

Table 4.1: Parameter values used in calculations

The mechanical resonant frequency, ratio of time constants, and threshold current densities for a particular device geometry are the important oscillator properties that are required. The general approach for designing a device is listed below.

- Calculate the resonator dimensions based on the desired frequency from equations in section 2.2

- Based on the actuator dimensions estimate the thermal time constant

- The threshold current density is obtained by calculating the threshold current through the actuator using eq. 2.41, and dividing by the cross sectional area of the actuator.

Calculated results for some Lamé mode, square extensional mode, disk wineglass mode, radial disk mode and ring extensional wineglass mode devices are listed in table 4.2. The width of the actuators is kept a constant ($1\ \mu m$) in all devices. As the ratio τ_M/τ_T deviates from the optimal value ($1/\sqrt{3}$), the threshold currents increase. The calculated values of threshold current densities hover around the breakdown current densities seen in silicon [37]. When current densities can be reached with no device degradation, frequencies much higher than currently attained (Hall et al. [2]) can be reached. The effect of scaling these devices can be observed visually on a contour plot of the threshold current density, as the actuator length and resonator dimensions

Device mode	D_M (μm)	L_T (μm)	f (MHz])	τ_T/τ_M	I_{th} (mA)	J_{th} (GA/m^2)
Lamé (2-supports)	$L:64.5$	1	60.22	0.46	4.03	2.69
		2		1.83	2.70	1.80
		3		4.11	2.99	1.99
Sq. ext. (4-supports)	$L:16.5$	1	301.3	2.28	10.47	3.49
		2		9.14	13.65	4.55
Disk WG (2-supports)	$R:4.1$	1	500.1	3.79	4.8	3.2
		2		15.16	6.58	4.38
		2.5		23.69	7.34	4.89
Disk radial (4-supports)	$R:5.9$	1	502.9	3.81	12.04	4.07
		1.5		8.57	14.36	4.78
		2.5		23.82	18.4	6.14
Ring EWG (4-supports)	$R_o:35$ $R_i:14$	1.1	210	1.93	14.4	4.8
		1.5		3.58	15.5	5.17
		2		6.36	17.4	5.81

Table 4.2: Calculated device performance chart

are varied. Figure 4-1 shows a contour plot of the threshold current density for a radial disk mode oscillator with 2-supports. The black curve traces the optimal time constant ratio ($\tau_M/\tau_T = 1/\sqrt{3}$, the red curve corresponds to $\tau_M/\tau_T = 1$, and the blue curve shows the design with a quarter wavelength actuator. For a given radius, the point of intersection with the black curve gives the optimal design for the smallest current requirements. This plot is made assuming a constant Q of 10,000. In reality the Q would vary based on the length of the actuators. It is also seen that the threshold current densities drop for larger devices, or lower frequencies.

4.2   Oscillator: Measurement Setup

Initiating sustained oscillations in these thermally-actuated oscillators requires a simple setup. The device is driven into spontaneous oscillations when a DC current running through the actuators exceeds the threshold current. The schematic of the oscillator characterization circuit is shown in Fig. 4-2. One end of the device is connected to the 'RF+DC' terminal of a bias-T capable of operating up to 2GHz and handling large currents. The DC current source driving the oscillator is connected to one end of the oscillator via the DC terminal of the bias-T, and the other end of
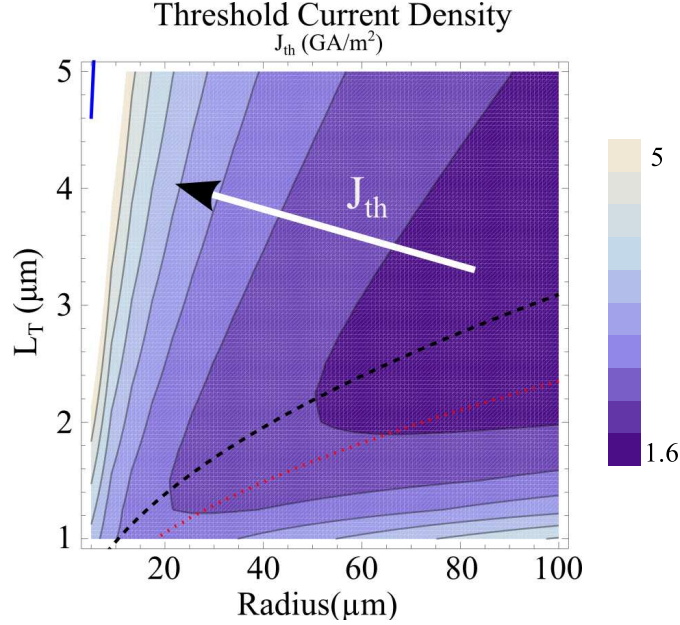
Figure 4-1: Threshold current density as the disk size (of the radial mode oscillator) and length of actuator are varied. The red, black and the blue curve (top left) map $\tau_M/\tau_T = 1$, $\tau_M/\tau_T = 1/\sqrt{3}$, and quarter wavelength actuator conditions respectively. For a particular radius, the intersection with the black curve gives the optimal actuator length.

the oscillator is grounded. After the onset of oscillations, a AC output plus the offset DC voltage (bias current times the total DC resistance of the path), appears at the 'RF+DC' terminal. The output of the oscillator is extracted through a capacitor, at the output of the RF terminal of the bias-T. The output spectrum is measured using an RF spectrum analyzer, and the waveforms can be recorded on an oscilloscope.

4.3   Experimental Results

The fabricated oscillators were tested on a vacuum probe station using the measurement setup shown in Fig. 4-2. The individual dies were mounted on a full wafer using copper tape and mounted on the chuck of the probe station where electrical connections were established using a GSG probe. For testing 4-contact devices, two GSG probes were used and connected to each other externally. The bias current from the current source was gradually increased in steps until oscillations were observed. The results presented here are from the first run of the fabrication process where
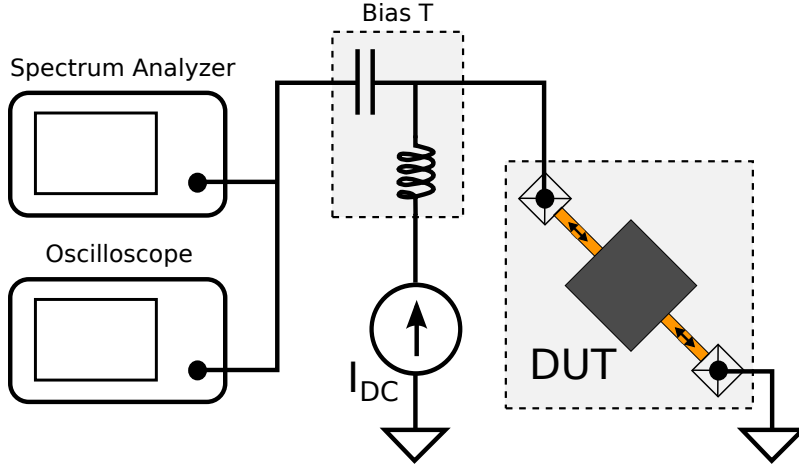
Figure 4-2: Schematic of the oscillator measurement circuit: a DC current source is connected to the device under test (DUT) through the DC terminal of the bias-T, and the oscillator output is read at the RF terminal of the bias-T.

the ion implantation steps were not included, as described in the previous chapter. An I-bar oscillator (similar to the device geometry reported in [2]) was tested first. The two proof masses are 8 μm × 12 μm and the four narrow beams are 3 μm long and 1 μm wide. The calculated threshold current is 3.38 mA. The device has a measured threshold current of 3.9mA and an oscillation frequency of 81.224 MHz. The spectrum of this mode was recorded at $I_{dc} = 4.1mA$, and is shown in Fig. 4-3. The additional bias current softens the actuators, and leads to a frequency reduction. At this bias current, the DC was measured to be 6.175 V. It was observed that the oscillations started instantly after crossing the threshold current.

Flexural mode oscillators based on the work by NXP Semiconductors [1], were also tested. For an oscillator with a 60 μm × 12 μm proof mass, 1 μm × 1 μm actuator, and 1 μm × 3 μm spring, the threshold current was observed to be 1.9 mA. Figure 4-4 shows the frequency spectrum observed with a 1.9 mA bias current a leading to a 2.37 V DC bias. The ability to make I-bar oscillators and flexural mode oscillators validates the overall process. These devices work at smaller threshold current densities and frequencies, which are easier to attain.

The various bulk mode devices described earlier were tested subsequently. A large fraction of devices were subjected to large current densities and these devices
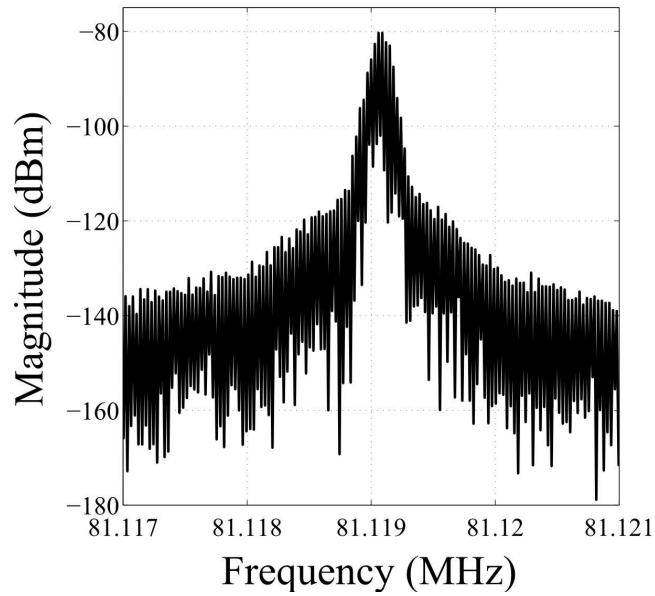
Figure 4-3: Observed frequency spectrum in an I-bar device($\sim$ [2]) with a 4.1 mA bias current. Proof mass dimensions: 8 μm $\times$ 12 μm, actuator dimensions: 3 μm $\times$ 1 μm.
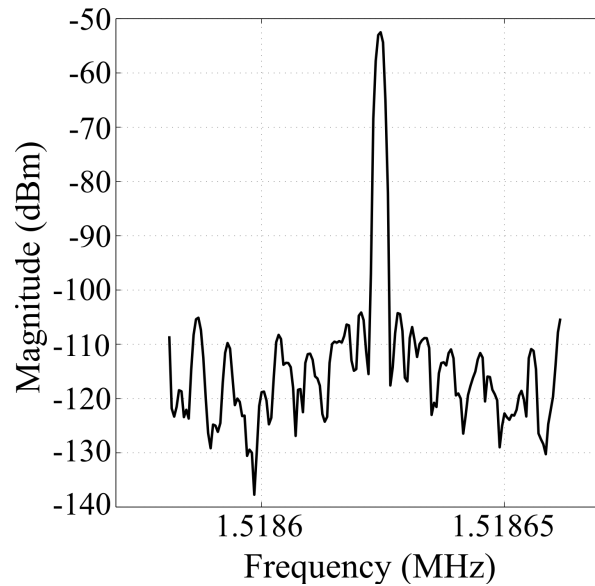
Figure 4-4: Frequency spectrum of a flexural mode oscillator at the oscillation threshold ($I_{dc} = 1.9\ mA$). Proof mass dimensions: 60 μm $\times$ 20 μm, actuator dimensions: 1 μm $\times$ 1 μm, spring dimensions: 1 μm $\times$ 3 μm.

failed before reaching the oscillation thresholds. High current densities in suspended structures leads to excessive Joule heating leading to breakdown [37]. The Lamé mode devices listed in the table 4.2 have the lowest threshold current density requirements. For design with $L_T = 2\ \mu m$, the time constant ratio by design is close to the optimal value. While slowly ramping up the bias current during testing, the device started oscillating at a bias current $I_{dc} = 2.27\ mA$, lesser that the predicted threshold current $(2.7\ mA)$. However, the dominant mode that was excited lies at 9.4 MHz, much below the Lamé mode frequency, and mostly any bulk mode frequency. Figure 4-5 shows the frequency spectrum observed in the absence of any bias current (in black), and with $I_{dc} = 2.27\ mA = I_{th}$ (in blue). It shows that the shallow peak close to 12 MHz is present in the absence of any bias current, and is likely a spurious noise point. There is also a negligible change in the noise floor at the resolution of this measurement data. The bias current was increased further to check for the occurrence of high frequency bulk modes, but these modes were not excited. Several harmonics of the excited mode were seen while looking at a wider frequency band. The frequency spectrum right before reaching the threshold of oscillations at a bias current $I_{dc} = 2.2\ mA\ (< I_{th})$, and right after surpassing the threshold with $I_{dc} = 2.3\ mA\ (> I_{th})$ are shown in Fig. 4-6. FEM simulations were performed on COMSOL to identify the probably mode shape of the measured mode. The results showed a cluster of several modes bunched around the measured frequency. Considering the possible uncertainty in the properties like the Young's modulus, and deviations of the actual device geometry from ideal shape it is hard to identify the probable mode shape. Measurements using characterization tools like the Laser Doppler Vibrometer (LDV) will provide insights into the actual mode shape and ways to suppress these undesired modes.

Among the bulk mode oscillators tested, most devices were tested until failure due to excessive current densities, and the remaining devices entered into sustained oscillations at low frequencies (possibly flexural modes) as described earlier. There are two important factors to be noted here. First, the devices tested so far belong to the first round of fabrication where contact implantation was not performed. The electrical contact to the devices (Ti/Al on top of silicon with $N_D\ \sim 1 \times 10^{18}/cm^3$)
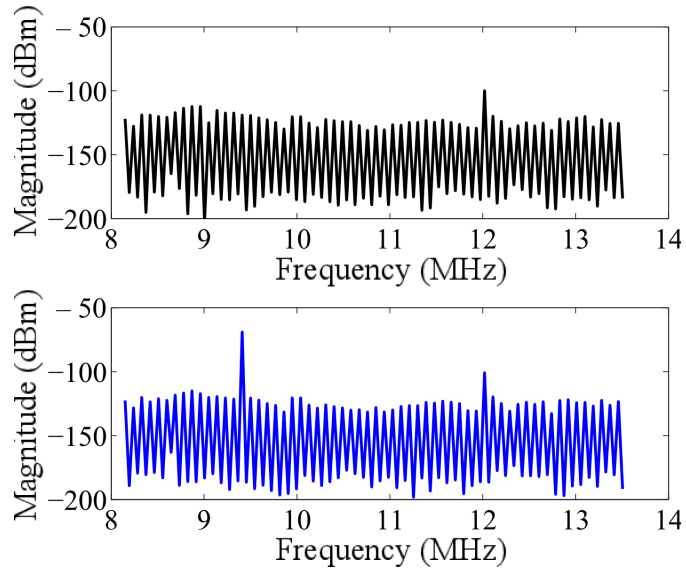
Figure 4-5: Frequency spectrum seen at the output of the Lamé mode device listed in table 4.2 with $L_T = 2 \ \mu m$. Black plot shows the measurement in the absence of any bias current, and the blue curve shows the spectrum at the onset of oscillations.
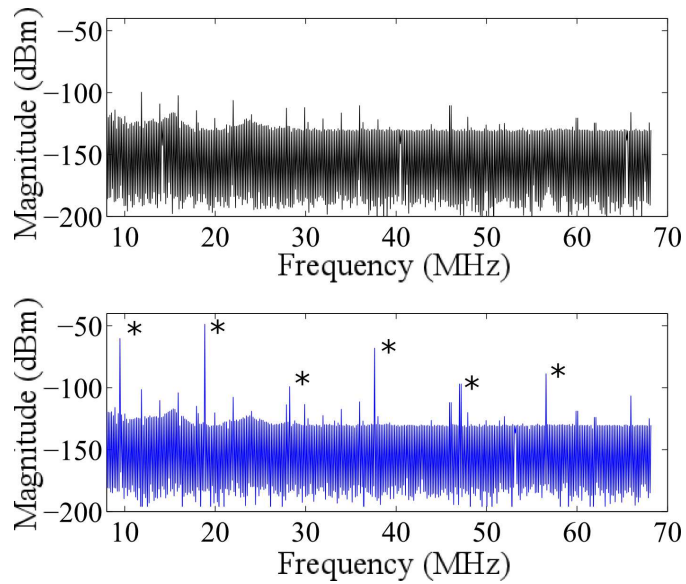
Figure 4-6: Frequency spectrum at the output of the Lamé mode device listed in table 4.2 with $L_T = 2 \ \mu m$ in the 8 MHz - 68 MHz band. The black curve shows the spectrum before the oscillation threshold of any mode is reached. Shallow peaks observed are mostly due to external noise. The spectrum at $I_{dc} = 2.3 \ mA \ (> I_{th})$ (in blue) shows several harmonics of the excited mode (marked '*').

500 μA/div

500 mV/div
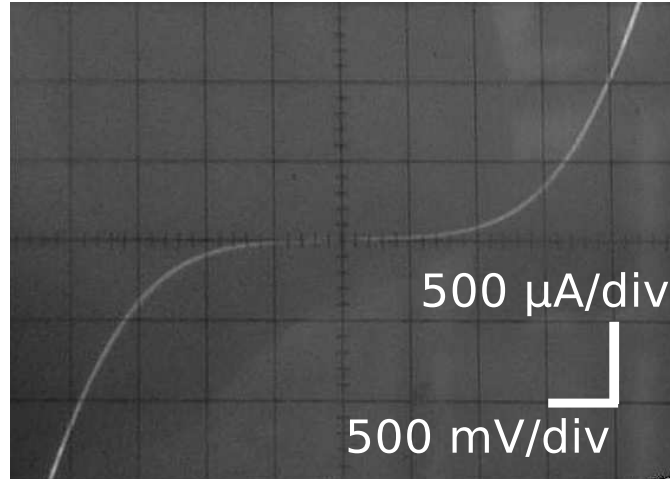
Figure 4-7: I - V characteristics of a rectangular bar defined in the device layer with two 100 μm × 100 μm contacts. The back to back diode like geometry causes symmetry in the characteristics.

turned out to be Schottky contacts. This is seen by the nonlinear diode-like behavior in the I-V characteristics below 2 V, shown in Fig 4-7. The device used for this measurement is a rectangular bar with two square contacts, and the symmetry in the characteristic occurs from having two back to back diodes. This diode like behavior of the contacts can be detrimental to the oscillator by limiting current flows or additional voltage drops and is undesirable. To overcome this problem, the contact region is being doped in next rounds of fabrication. Second, the devices tested here were plagued by problems while removing the thick resist used in the last lithography step of the process. These resist patches affect the proof mass severely in bulk mode devices unlike flexural mode devices where the proof mass is not subjected to repeated stresses. As a result, the Q of the bulk modes can be significantly degraded causing flexural modes to be more favorable compared to bulk modes These two problems are being corrected in the new fabrication process.

Chapter 5

Summary and Future Work

Thermally-actuated and piezoresistively-sensed oscillators described here are promising due to the lack of need for additional electronics, normally required to build oscillators. There is an important need to push the performance of these oscillators further, to higher frequencies and lower powers. To achieve this, the thesis starts with a fundamental analysis of the oscillators to understand the key factors responsible for improving the performance. Based on this, the interplay between the thermal and mechanical time constants is found to be crucial. The optimal value of τ_M/τ_T is found to be $1/\sqrt{3}$. It is also found that the threshold current density required for oscillations increases with frequency ($\propto \omega_0^{0.25}$). Several bulk mode oscillators were designed, fabricated at the MTL cleanroom, and tested. A fraction of the bulk mode oscillators tested were subjected to large current densities and suffered from structural damage due to excessive heat. Other oscillators settled into other low frequency modes that could be sustained at lower threshold current densities compared to the bulk modes they were designed for. Improvements were made to the first fabrication process based on results presented here, and new processes are being tested. There are several directions for future work to improve the oscillators studied here

- One of the principal requirements for the oscillator designs used here is the ability to engineer them to pick the desired mode for oscillations. Investigation on techniques to pick the intended mode and suppress undesired low -f modes

would extremely beneficial.

- Once devices can be forced to oscillate in the desired mode repeatably, it is important to probe the upper limits of f attainable with these devices. Reaching higher frequencies without increasing the power requirements will be a significant challenge.

- These oscillators carry large currents and frequency tuning is currently performed by varying the current, causing a change in the temperature and hence the Young's modulus. Exploring active methods of tuning that are decoupled from the bias current can be useful. Varying a large bias current repeatedly for tuning can be challenging when the current source is implemented on chip.

- With no need for additional amplifiers, these oscillators could be an interesting platform for studying the fundamentals of coupled oscillators.

- An experimental investigation of the jitter performance of these oscillators has been reported [38] however, no work has been performed to study the phase noise limits of these oscillators compared to other prominent oscillators.

- The analytical framework developed here for optimizing the device design was performed by assuming that the thermal time constant can be varied independent of the Q. It will be interesting to investigate how changes in the actuator length affect the quality factor. Then the benefits from tailoring the actuator length for optimizing the actuation efficiency can be weighed against the improvements arising by optimizing the actuator lengths for improved quality factors. This analysis will be useful in making realistic judgements on reducing the current consumption.

70

Appendix A

Tables

Variable	Description
A	Area of cross-section $[m^2]$
A_T	Area of cross-section of the thermal actuator $[m^2]$
b	Damping constant $[Kg/s]$
C_m	Lumped equivalent mechanical capacitance $[m/N]$
C_p	Specific heat capacity $[J/Kg - K]$
C_t	Equivalent thermal capacitance $[J/K]$
D_M	Dominant planar resonant dimension $[m]$
E	Young's modulus $[Pa]$
f	Frequency $[Hz]$
F	Force $[N]$
I	Current $[A]$
I_{dc}	Constant bias current in the oscillator $[A]$
I_{th}	Threshold current for oscillations $[A]$
$I_{th,density}$	Threshold current density for oscillations $[A/m^2]$
J	Current density $[A/m^2]$
J_{th}	Threshold current density $[A/m^2]$
k	Spring stiffness of 1-DOF system $[N/m]$
k_{th}	Thermal conductivity $[W/m - K]$

K	Effective stiffness of the resonator $[N/m]$
K_t	Actual longitudinal stiffness of the actuator $[N/m]$
K_{eff}	Effective stiffness$[N/m]$
K'	Equivalent stiffness of the thermal actuator $[N/m]$
L	Length $[m]$
L_T	Length of the thermal actuator $[m]$
L_m	Lumped equivalent mechanical inductance $[Kg]$
m	Mass of a 1-DOF system $[Kg]$
M_{eff}	Effective mass$[Kg]$
n	Mode number
n_{el}	Effective number of series supports in current path
P_{ac}	Joule heating power $[W]$
P_{th}	Thermal power $[W]$
Q	Quality factor
Q_h	Thermal energy stored $[J]$
r	Radial coordinate $[m]$
r_{ac}	Resistance variation (AC) due to the piezoresistive effect $[\Omega]$
R	Radius of the disk $[m]$
R_{dc}	Resistance of the structure $[\Omega]$
R_e	Electrical resistance $[\Omega]$
R_i	Inner radius of the ring $[m]$
R_m	Lumped equivalent mechanical resistance $[Kg.rad/s]$
R_o	Outer radius of the ring $[m]$
R_t	Equivalent thermal resistance $[K/W]$
t	Thickness $[m]$
T	Temperature $[K]$
ΔT	Temperature change $[K]$
T_p	Spatial-peak AC temperature $[K]$
T_M	Thickness (mechanical) $[m]$

U	Radial displacement $[m]$
V	Tangential displacement $[m]$
V_{ac}	AC voltage (oscillator output) $[V]$
x	Displacement of the resonator $[m]$
x_{EM}	Effective mass coefficient
α	Thermal expansion coefficient (length adjusted) $[mK^{-1}]$
α_t	Normalized thermal expansion coefficient $[K^{-1}]$
β_{mode}	Modal coefficient of frequency
θ	Angular coordinate $[rad]$
ν	Poisson's ratio
π_l	Longitudinal piezoresistive coefficient $[Pa^{-1}]$
$\pi_{\alpha\beta}$	Component of piezoresistive coefficient tensor $[Pa^{-1}]$
ρ	Density $[Kg/m^3]$
ρ_e	Electrical resistivity $[\Omega m]$
ρ_M	Density (mechanical) $[Kg/m^3]$
$\Delta\rho_{e\alpha}$	Change in resistivity $[\Omega m]$
τ_M	Mechanical time-constant $[s/rad]$
τ_T	Thermal time-constant $[s]$
ϕ_M	Phase shift from mechanical elements $[rad]$
ϕ_T	Phase shift from thermal components $[rad]$
σ_e	Electrical conductivity $[\mho/m]$
σ_β	Component of stress tensor $[Pa]$
ω	Frequency of oscillation $[rad/s]$
ω_0	Mechanical resonant frequency $[rad/s]$

Table A.1: List of all variables

Bibliography

[1] K. L. Phan, P. G. Steeneken, M. J. Goossens, G. E. J. Koops, G. J. A. M. Verheijden, and J. T. M. van Beek, "Spontaneous mechanical oscillation of a DC driven single crystal," *ArXiv e-prints*, Apr. 2009.

[2] H. Hall, D. Walker, L. Wang, R. Fitch, J. Bunch, S. Pourkamali, and V. Bright, "Mode selection behavior of VHF thermal-piezoresistive self-sustained oscillators," in *Solid-State Sensors, Actuators and Microsystems (TRANSDUCERS & EUROSENSORS XXVII), 2013 The 17th International Conference on*. IEEE, 2013, pp. 1392–1395.

[3] H. Baltes, O. Brand, G. K. Fedder, C. Hierold, J. G. Korvink, and O. Tabata, *CMOS-MEMS: Advanced Micro and Nanosystems*. John Wiley & Sons, 2008.

[4] C.-C. Nguyen, "MEMS technology for timing and frequency control," *Ultrasonics, Ferroelectrics and Frequency Control, IEEE Transactions on*, vol. 54, no. 2, pp. 251–270, 2007.

[5] C.-C. Nguyen and R. T. Howe, "An integrated CMOS micromechanical resonator high-q oscillator," *Solid-State Circuits, IEEE Journal of*, vol. 34, no. 4, pp. 440–455, 1999.

[6] A. Nelson, J. Hu, J. Kaitila, R. Ruby, and B. Otis, "A 22μw, 2.0 GHz FBAR oscillator," in *Radio Frequency Integrated Circuits Symposium (RFIC), 2011 IEEE*. IEEE, 2011, pp. 1–4.

[7] J. T. M. Van Beek and R. Puers, "A review of MEMS oscillators for frequency reference and timing applications," *Journal of Micromechanics and Microengineering*, vol. 22, no. 1, p. 013001, 2012.

[8] G. K. Ho, K. Sundaresan, S. Pourkamali, and F. Ayazi, "Low-motional-impedance highly-tunable, I^2 resonators for temperature compensated reference oscillators," *MEMS05*, 2005.

[9] A. Samarao, G. Casinovi, and F. Ayazi, "Passive TCF compensation in high Q silicon micromechanical resonators," in *Micro Electro Mechanical Systems (MEMS), 2010 IEEE 23rd International Conference on*. IEEE, 2010, pp. 116–119.

[10] V. Kaajakari, T. Mattila, A. Oja, and H. Seppa, "Nonlinear limits for single-crystal silicon microresonators," *Microelectromechanical Systems, Journal of*, vol. 13, no. 5, pp. 715–724, 2004.

[11] P. G. Steeneken, K. Le Phan, M. J. Goossens, G. E. J. Koops, G. J. A. M. Brom, C. Van der Avoort, and J. T. M. Van Beek, "Piezoresistive heat engine and refrigerator," *Nature Physics*, vol. 7, no. 4, pp. 354–359, 2011.

[12] A. Rahafrooz and S. Pourkamali, "Fully micromechanical piezo-thermal oscillators," in *Electron Devices Meeting (IEDM), 2010 IEEE International*, 2010, pp. 7.2.1–7.2.4.

[13] ——, "High frequency dual-mode thermal-piezoresistive oscillators," in *Frequency Control and the European Frequency and Time Forum (FCS), 2011 Joint Conference of the IEEE International*. IEEE, 2011, pp. 1–4.

[14] X. Guo, Y. bo Yi, and S. Pourkamali, "Thermal-piezoresistive resonators and self-sustained oscillators for gas recognition and pressure sensing," *Sensors Journal, IEEE*, vol. 13, no. 8, pp. 2863–2872, 2013.

[15] C. S. Smith, "Piezoresistance effect in germanium and silicon," *Phys. Rev.*, vol. 94, pp. 42–49, Apr 1954. [Online]. Available: http://link.aps.org/doi/10.1103/PhysRev.94.42

[16] P. Regoliosi, A. Reale, A. Di Carlo, S. Orlanducci, M. L. Terranova, and P. Lugli, "Piezoresistive behaviour of single wall carbon nanotubes," in *Nanotechnology, 2004. 4th IEEE Conference on*. IEEE, 2004, pp. 149–151.

[17] R. He and P. Yang, "Giant piezoresistance effect in silicon nanowires," *Nature nanotechnology*, vol. 1, no. 1, pp. 42–46, 2006.

[18] Y. Kanda, "A graphical representation of the piezoresistance coefficients in silicon," *Electron Devices, IEEE Transactions on*, vol. 29, no. 1, pp. 64–70, 1982.

[19] ——, "Piezoresistance effect of silicon," *Sensors and Actuators A: Physical*, vol. 28, no. 2, pp. 83 – 91, 1991. [Online]. Available: http://www.sciencedirect.com/science/article/pii/092442479185017I

[20] K. Matsuda, K. Suzuki, K. Yamamura, and Y. Kanda, "Nonlinear piezoresistance effects in silicon," *Journal of Applied Physics*, vol. 73, no. 4, pp. 1838–1847, 1993.

[21] H. Watanabe, N. Yamada, and M. Okaji, "Linear thermal expansion coefficient of silicon from 293 to 1000 K," *International Journal of Thermophysics*, vol. 25, no. 1, pp. 221–236, 2004. [Online]. Available: http://dx.doi.org/10.1023/B%3AIJOT.0000022336.83719.43

[22] E. Hwang and S. A. Bhave, "PN-diode transduced 3.7-GHz silicon resonator," in *Micro Electro Mechanical Systems (MEMS), 2010 IEEE 23rd International Conference on*. IEEE, 2010, pp. 208–211.

[23] R. Lifshitz and M. L. Roukes, "Thermoelastic damping in micro-and nanomechanical systems," *Physical review B*, vol. 61, no. 8, p. 5600, 2000.

[24] M. Shahmohammadi, B. P. Harrington, and R. Abdolvand, "Concurrent enhancement of Q and power handling in multi-tether high-order extensional resonators," in *Microwave Symposium Digest (MTT), 2010 IEEE MTT-S International.* IEEE, 2010, pp. 1452–1455.

[25] B. Harrington and R. Abdolvand, "Q-enhancement through minimization of acoustic energy radiation in micromachined lateral-mode resonators," in *Solid-State Sensors, Actuators and Microsystems Conference, 2009. TRANSDUCERS 2009. International.* IEEE, 2009, pp. 700–703.

[26] V. Kaajakari, T. Mattila, A. Oja, J. Kiihamaki, and H. Seppa, "Square-extensional mode single-crystal silicon micromechanical resonator for low-phase-noise oscillator applications," *Electron Device Letters, IEEE*, vol. 25, no. 4, pp. 173–175, 2004.

[27] K. Nakamura and K. Kumasaka, "Lame-mode piezoelectric resonators and transformers using LiNbO$_3$ crystals," in *Ultrasonics Symposium, 1995. Proceedings., 1995 IEEE*, vol. 2. IEEE, 1995, pp. 999–1002.

[28] M. Onoe, "Contour vibrations of isotropic circular plates," *the Journal of the Acoustical Society of America*, vol. 28, p. 1158, 1956.

[29] M. A. Abdelmoneum, M. U. Demirci, and C.-C. Nguyen, "Stemless wine-glass-mode disk micromechanical resonators," in *Micro Electro Mechanical Systems, 2003. MEMS-03 Kyoto. IEEE The Sixteenth Annual International Conference on.* IEEE, 2003, pp. 698–701.

[30] G. Ambati, J. Bell, and J. Sharp, "In-plane vibrations of annular rings," *Journal of Sound and Vibration*, vol. 47, no. 3, pp. 415–432, 1976.

[31] Y. Xie, S.-S. Li, Y.-W. Lin, Z. Ren, and C.-C. Nguyen, "1.52-GHz micromechanical extensional wine-glass mode ring resonators," *Ultrasonics, Ferroelectrics and Frequency Control, IEEE Transactions on*, vol. 55, no. 4, pp. 890–907, 2008.

[32] S. A. Bhave, D. Gao, R. Maboudian, and R. T. Howe, "Fully-differential poly-SiC lame mode resonator and checkerboard filter," in *Micro Electro Mechanical Systems, 2005. 18th IEEE International Conference on.* IEEE, 2005, pp. 223–226.

[33] J. R. Clark, W.-T. Hsu, M. A. Abdelmoneum, and C.-C. Nguyen, "High-Q UHF micromechanical radial-contour mode disk resonators," *Microelectromechanical Systems, Journal of*, vol. 14, no. 6, pp. 1298–1310, 2005.

[34] R. A. Johnson, *Mechanical filters in electronics.* Wiley New York, 1983.

[35] T. L. Bergman, A. S. Lavine, F. P. Incropera, and D. P. Dewitt, *Introduction to heat transfer*. John Wiley & Sons, Incorporated, 2011.

[36] K. R. Williams, K. Gupta, and M. Wasilik, "Etch rates for micromachining processing-part II," *Microelectromechanical Systems, Journal of*, vol. 12, no. 6, pp. 761–778, 2003.

[37] J. Wurz, L. VJ, A. Sarkar, and I. Saif, "High current density and failure mechanism in epitaxially bridged silicon nanowires," in *Nanotechnology, 2008. NANO'08. 8th IEEE Conference on.* IEEE, 2008, pp. 595–597.

[38] A. Rahafrooz and S. Pourkamali, "Jitter characterization of fully-micromechanical thermal-piezoresistive oscillators," in *Frequency Control Symposium (FCS), 2012 IEEE International.* IEEE, 2012, pp. 1–4.